Journal of Asian Earth Sciences 116 (2016) 1–25

Contents lists available at ScienceDirect

Journal of Asian Earth Sciences

journal homepage: www.elsevier.com/locate/jseaes

Geological characteristics and age of the Dahongliutan Fe-ore deposit in the Western Kunlun orogenic belt, Xinjiang, northwestern China

Jun Hu [a,c], He Wang [a,*], Chaoyang Huang [d], Laixi Tong [b], Shenglu Mu [a,c], Zengwang Qiu [a,c]

[a] Key Laboratory of Mineralogy and Metallogeny, Guangzhou Institute of Geochemistry, Chinese Academy of Sciences, Guangzhou 510640, China
[b] State Key Laboratory of Isotope Geochemistry, Guangzhou Institute of Geochemistry, Chinese Academy of Sciences, Guangzhou 510640, China
[c] University of Chinese Academy of Sciences, Beijing 100049, China
[d] Institute of Engineering, Chongqing 402260, China

ARTICLE INFO

Article history:
Received 4 January 2015
Received in revised form 6 August 2015
Accepted 11 August 2015
Available online 12 August 2015

Keywords:
Superior-type BIF
Neoproterozoic–Early Cambrian
Dahongliutan Fe deposit
Tianshuihai terrane
Western Kunlun orogenic belt

ABSTRACT

The large-scale Dahongliutan hematite-rich Fe deposit in the Tianshuihai terrane (Western Kunlun orogenic belt), Xinjiang, northwestern China, contains proven Fe ore reserves exceeding 100 Mt at an average grade of 35 wt.% Fe(t) (maximum 53 wt.%). The deposit is hosted in the Neoproterozoic Tianshuihai Group, a suite of neritic, siliciclastic and sedimentary carbonate rocks subjected to greenschist-facies metamorphism. The Fe orebodies are laminate, stratoid, lenticular and interlayered with marbles and schists. Ore minerals mainly contain hematite, with minor siderite and limonite and rare sulfides, whereas gangue minerals mainly comprise quartz, dolomite, ankerite, calcite, muscovite and chloritoid. Most Fe ores display lepidoblastic, blastopsammitic, crystalloblastic and metasomatic textures with massive or banded structures. Based on mineral assemblages, the Fe ores are divided into four types, namely: (1) Quartz–hematite; (2) Quartz–dolomite–calcite–muscovite–hematite; (3) Quartz–ankerite–hematite; (4) Quartz–siderite–hematite.

Zircon U–Pb analyses on the marbles and schists yielded a Neoproterozoic age (Ediacaran; 593 ± 7 Ma), whereas those on the ore-intruding medium-grained porphyritic biotite-quartz monzonite, medium to fine grained biotite-quartz monzonite and metagabbro yielded Cambrian–Early Ordovician ages (i.e., 484.5 ± 2.7, 527.9 ± 2.8 and 532.3 ± 3.1 Ma), which altogether constrain the ore formation to the Late Neoproterozoic to Early Cambrian (532–593 Ma). In addition, the 163 detrital zircon analyses on the Dahongliutan marble and schist define five major age populations, namely: 2561–2329, 2076–1644, 1164–899, 869–722 and 696–593 Ma. Provenance studies show that the detritals at Dahongliutan were mainly sourced from the North Kunlun and Tianshuihai terranes.

Comparison with typical BIF deposits in the world, we infer that the deposit belongs to Neoproterozoic (Ediacaran) BIF-related sedimentary metamorphic type iron deposit and resembles Superior-type BIF, probably reflecting the recurrence of anoxic ferruginous conditions in the Neoproterozoic–Early Cambrian deep sea.

1. Introduction

The Western Kunlun orogenic belt, located along the northern periphery of the Tibetan plateau (Fig. 1a), represents a key tectonic junction between the Pan-Asia and the Tethyan tectonic domains. Its tectonic evolution was closely related to the subduction of the Proto- and Paleo-Tethys and the collision of the Early Paleozoic to Early Mesozoic terranes (Mattern and Schneider, 2000; Xiao et al., 2002, 2003; Jiang et al., 2013), and Cenozoic deformation by the far-field effects of the India–Asia collision (Matte et al., 1996; Kao et al., 2001; Xiao et al., 2002). This orogenic belt contains Precambrian to Cenozoic sedimentary rocks, as well as numerous igneous and metamorphic rock units, which reflect the immense complexity of its tectonic assemblages, from magmatic arc, to Mid-Ocean Ridge, to back-arc basin settings (Dong et al., 2004; Pirajno, 2013). The long-term complex geological evolution had facilitated the formation of a wide variety of ore systems, notably sedimentary Fe (or BIFs), porphyry Cu–Mo, volcanogenic massive sulfides (VMS) and Mississippi Valley-Type (MVT) Pb–Zn deposits (Kuang et al., 2002; Dong et al., 2004; Xiao et al., 2006; Liu et al., 2010; Yan et al., 2012; Chen et al., 2013; Pirajno, 2013; Huang, 2014). In particular, in the Precambrian strata in the western segment of the Tianshuihai terrane, several large-scale magnetite-rich

* Corresponding author.
E-mail address: wanghe@gig.ac.cn (H. Wang).

http://dx.doi.org/10.1016/j.jseaes.2015.08.014
1367-9120/

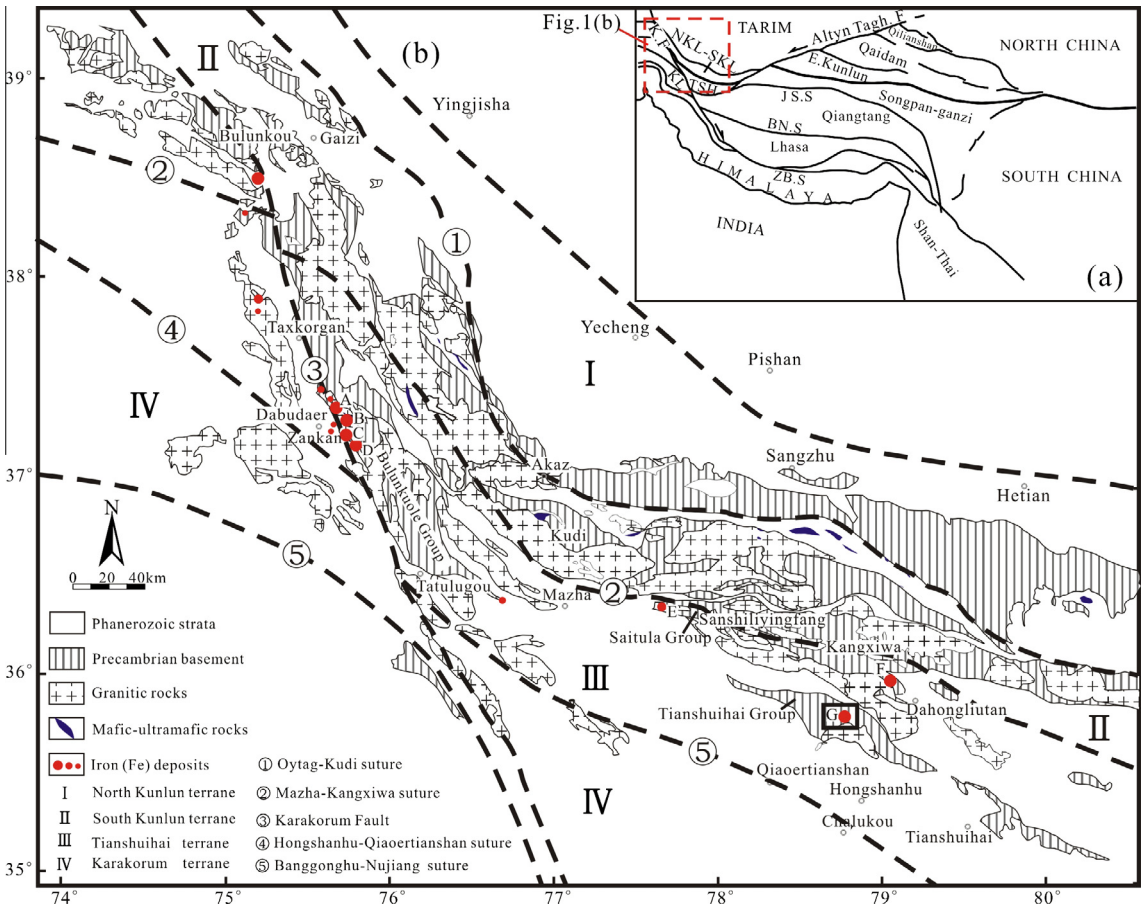

Fig. 1. (a) Regional map (after Pan et al., 2004; Xiao et al., 2005) and (b) simplified geological map of the Western Kunlun orogenic belt, Xinjiang, northwestern China (after Dong et al., 2004; Pan et al., 2004; Huang, 2014). In (a): NKL = North Kunlun terrane, SKL = South Kunlun terrane, TSH = Tianshuihai terrane, KL = Karakorum terrane, K. F = Karakorum Fault, JS. S = Jinsha Suture, BN. S = Banggong–Nujiang suture, ZB. S = Zangbo Suture; In (b): A = Yelike Fe deposit, B = Laobing Fe deposit, C = Zankan Fe deposit, D = Mokaer Fe deposit, E = Heiheizigan Fe deposit, F = Akesayi Fe deposit, G = Dahongliutan Fe deposit.

Fe deposits (e.g., Zankan, Yelike, Laobing and Mokaer Fe deposits) have been discovered (Yan et al., 2012; Chen et al., 2013; Huang, 2014) (Fig. 1b). In addition, the Heiheizigan and Akesayi hematite-rich ore Fe deposits were discovered in the eastern segment of the Tianshuihai terrane (Fig. 1b).

The Dahongliutan Fe-ore deposit is a large-scale deposit, which has been prospected by the Xinjiang Xindi Geological Exploration Company since 2007, in the eastern segment of the Tianshuihai terrane (Fig. 1b), with the proven Fe ore reserves exceeding 100 Mt, at an average grade of 35 wt.% Fe(t) (maximum 53 wt.%). This deposit is hosted in a suite of greenschist facies-metamorphosed, shallow marine siliciclastic and sedimentary carbonate rocks. This deposit comprises hematite-rich Fe-ores, locally with siderite-rich and limonite-rich Fe-ores, with rare sulfides, as well as quartz, ankerite, calcite, dolomite, muscovite, chloritoid. Previous research on this deposit is very poor due to geographic remoteness and bad road access.

In this paper, we present the first detailed description on the geological characteristics of the Dahongliutan deposit, including its host rocks, ore-controlling structures, metamorphism, ore and gangue minerals, ore texture and structure; then we provide data of the first LA-ICP-MS zircon U–Pb ages from the intrusive rocks and metamorphic siliciclastic and sedimentary carbonate rocks at Dahongliutan, which allow us to better constrain the detrital source areas and the age of deposition of both the sediments and the Fe deposit hosted by them. After this, we compare the Dahongliutan Fe deposit with typical BIF deposits in the world, and discuss the ore deposit type.

2. Regional geology

The Western Kunlun orogenic belt is located between the Tarim Block to the north and the Tibetan Plateau to the southeast (Fig. 1a). From north to south, the belt is subdivided into the North Kunlun, South Kunlun, Tianshuihai and Karakorum terranes separated by the Oytag–Kudi suture, Mazar–Kangxiwar suture and Hongshanhu–Qiaoertianshan suture, respectively (Fig. 1b) (Pan, 1996; Jiang et al., 2002; Pan et al., 2004; Zhang et al., 2007).

The basement of the North Kunlun terrane, as the southern continuation of the Tarim Craton, is dominated by the Archean to Paleoproterozoic gneisses, migmatites, amphibolites and schists intruded by the Paleoproterozoic (ca. 2.42–2.2 Ga) Akaz–Xuxugou granites. The protoliths to the Precambrian metamorphic rocks had undergone amphibolite facies metamorphism in the Neoproterozoic (ca. 1.0–0.9 and 0.8 Ga) (Matte et al., 1996; Yuan et al., 2002, 2003; Xiao et al., 2003; Zhang et al., 2003a, 2007). The basement is overlain by a low-grade metamorphosed Upper Neoproterozoic (Sinian; ca. 800–570 Ma) succession of laminated carbonates, volcanics, shales, marls and tuffites, which are well-exposed around the Akaz Pass (Mattern and Schneider, 2000). The laminated carbonates (parallel-bedded limestone and

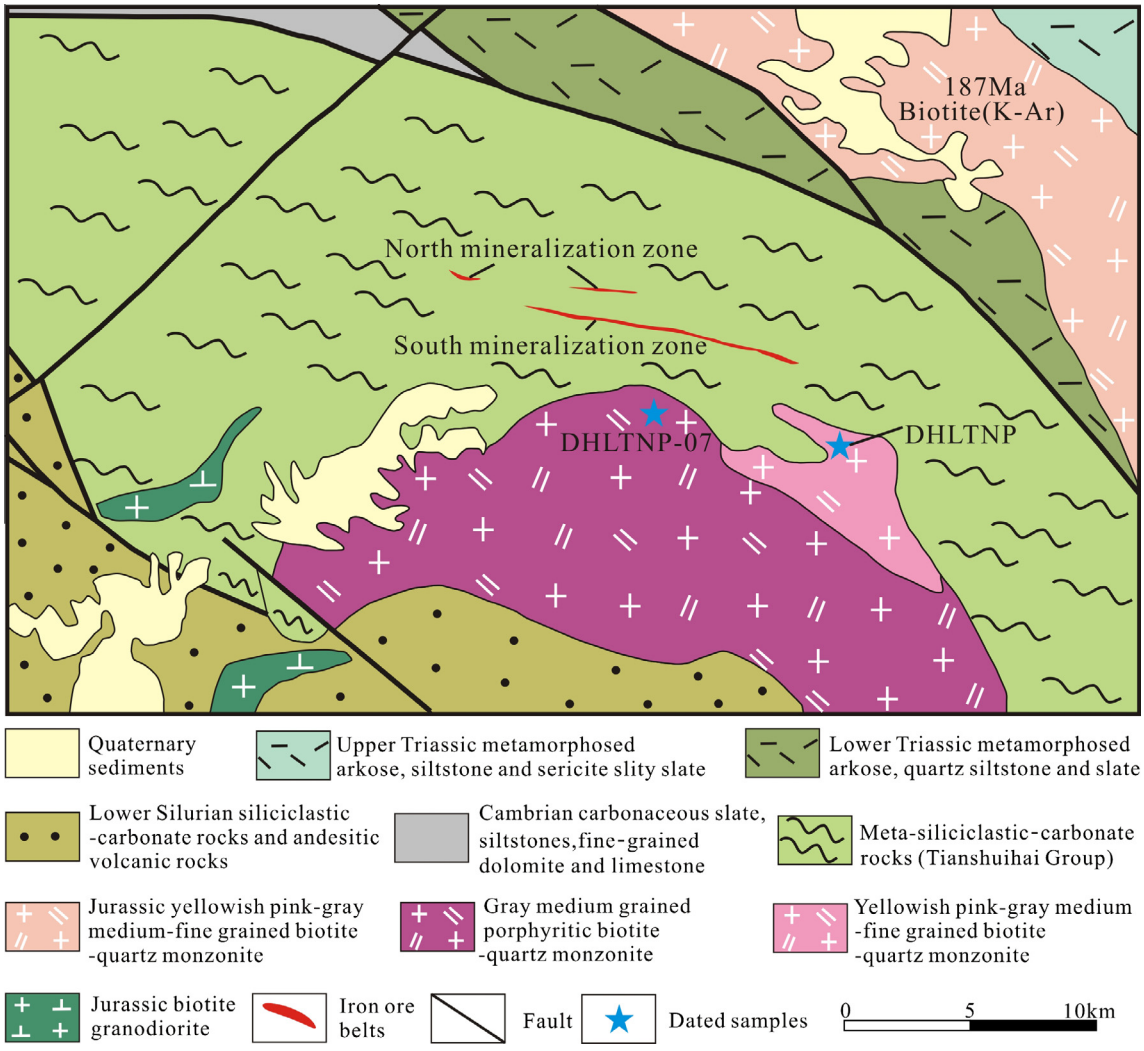

Fig. 2. Simplified geological map of the Dahongliutan Fe mining district and its adjacent area (after Geological Survey Academy of Shaanxi Province, 2006).

dolomite) indicate a shallow marine depositional environment (Mattern and Schneider, 2000). According to Pan (1996), the metavolcanics are former oceanic tholeiites. Therefore, the Sinian succession was interpreted as a rift sequence formed during the fragmentation of a shallow marine platform (Mattern et al., 1996; Pan, 1996). With the development of the Sinian rifting, ocean spreading might have taken place during the later Sinian to Early Paleozoic, which resulted in the formation of the Proto-Tethys Ocean whose remnants are found at the Oytag–Kudi suture (Pan, 1996; Mattern and Schneider, 2000). South-dipping subduction of the Proto–Tethyan oceanic crust during the Early Paleozoic (Late Cambrian to earliest Ordovician) may have generated an early Paleozoic granitoid belt that is preserved in the South Kunlun terrane close to the Oytag–Kudi suture (Xiao et al., 2002, 2005; Jiang et al., 2002, 2013). This subduction may have led to accretion of the arc onto the North Kunlun terrane, creating an active continental margin with north-dipping subduction underneath (Xiao et al., 2002). It has been suggested that the collision between the North Kunlun and South Kunlun terranes might have occurred in the Silurian (Pan, 1996; Mattern and Schneider, 2000; Jiang et al., 2013), resulting in the closure of the Proto-Tethyan ocean (Mattern et al., 1996; Pan, 1996).

The South Kunlun terrane consists of a Mesoproterozoic metamorphic complex primarily composed of schist and gneiss locally intercalated with ultramafic lenses (Gaetani et al., 1990; Zhou, 1998), which is lithologically similar to the basement of the North Kunlun terrane (Yuan et al., 2002, 2003). The overlying strata are dominated by Upper Paleozoic to Mesozoic siliciclastic-, carbonate- and calc-alkaline volcanic rocks (Pan et al., 1994; Pan, 1996). Phanerozoic strata, except the Silurian to Middle Devonian ones, are widespread in the North Kunlun and South Kunlun terranes. Granitoids are mainly of Late Paleozoic to Late Triassic ages (Jiang et al., 2002, 2013).

The Tianshuihai terrane is a NW–SE trending belt extending from the Mazar–Kangxiwar suture in the north to the Qianertianshan–Hongshanhu suture in the south (Fig. 1b). Knowledge of the Tianshuihai geology remains sparse and due to geographic remoteness and widespread glacial coverage (Yuan et al., 2002). As a result, there have been different views on the regional geological evolution. For example, Xiao et al. (2005) and Liu et al. (2015) favoured Tianshuihai to be the western extension of the Songpan–Ganzi block which collided with the South Kunlun terrane in the Early Mesozoic. However, Yuan et al. (2003) and Zhang et al. (2007) proposed that Tianshuihai was part of the South Kunlun terrane. Many large-scale sedimentary–metamorphic Fe deposits have been discovered in the Precambrian strata of the Tianshuihai terrane, notably the Zankan, Yelike, Laobing and Mokaer magnetite deposits in the Bulunkuole Group (Fig. 1b) (Chen et al., 2013), as well as the Heiheizigan and Akesayi hematite–magnetite deposits (Fig. 1b) in the Saitula Group (Wang, 1983; Li et al., 2008). The

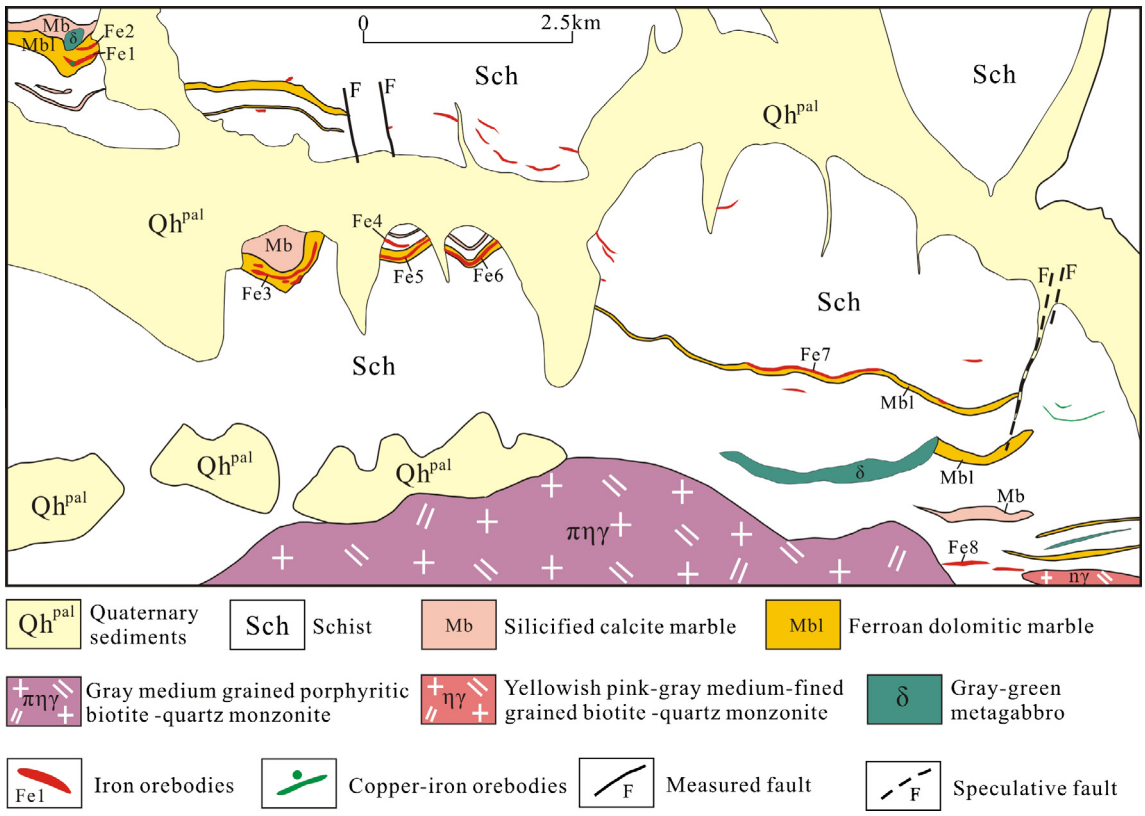

Fig. 3. Geological map of the Dahongliutan deposit.

amphibolite-facies metamorphosed Bulunkuole Group comprises mainly biotite-plagioclase gneiss interbedded with plagioclase-amphibolite schist, sillimanite-garnet gneiss and marble. The protoliths of the Bulunkuole metamorphic rocks can be recognized as a suite of volcaniclastic and sedimentary carbonate sequence (Huang, 2014). The depositional age of the Bulunkuole Group remains controversial: (1) Inherited zircon ages of 600–2200 Ma from two gneiss samples nearby Taxkorgan suggest that the deposition of the Bulunkuole Group occurred between Neoproterozoic and Early Paleozoic (Zhang et al., 2007); (2) Zircon U–Pb ages of 2130–2700 Ma have been reported on the metamorphic rocks comparable to those of the Bulunkuole Group, in western Pamir syntaxis (Wang, 2008); (3) U–Pb zircon age of 2481 ± 14 Ma has been reported from volcanic rocks in the Bulunkuole Group located west of Taxkorgan (Ji et al., 2011); (4) U–Pb zircon dating of biotite quartz schist, felsic schist and plagioclase amphibole schist from Zankan, Yelike, Laobing and Zankandong Fe deposits show that the Bulunkuole Group was formed at 510–540 Ma and metamorphosed at 463–480 Ma (Yan et al., 2012; Huang, 2014). The greenschist to amphibolite-facies metamorphosed Saitula Group (Fig. 1b) consists of biotite-plagioclase gneiss, biotite-muscovite-plagioclase gneiss, garnet-quartz schist and quartzite-amphibolite schist and marble. The protoliths of the Saitula Group were clastic sedimentary rocks with small amount of sedimentary carbonates and mafic volcanic rocks (Li et al., 2008). Wang (1983) and Li et al. (2008) suggested the Mesoproterozoic depositional age for the Sailatu Group based on the Rb–Sr whole-rock isochron age of 1576 Ma for the emplaced granites. Early Paleozoic magmatic and metamorphic events and the Early Jurassic (Yanshanian) granitoids are widespread in the Tianshuihai terrane (Jiang et al., 2002).

The Karakorum terrane is located between the Hongshanhu–Qianertianshan suture in the north and the Bangonghu–Nujiang suture in the south. This terrane includes Cambrian/Ordovician to Triassic strata (Matte et al., 1992; Pan, 1996) characterized by the occurrence of thick monotonous and partly metamorphosed successions of marine clastic deposits exhibiting a flyschoid character (Mattern and Schneider, 2000). The sedimentary facies character of these clastic deposits (e.g. siliciclastic turbidites, allodapic limestone beds), compositional aspects (granitoid debris) as well as the occurrence of tuffites can be reconciled with an active margin setting and is in support of the Late Triassic–Early Jurassic accretionary wedge interpretation (Mattern and Schneider, 2000; Xiao et al., 2005).

The Dahongliutan Fe-ore deposit is hosted in the Tianshuihai Group in the eastern Tianshuihai terrane (Figs. 1b and 2). Cui et al. (2005) discovered Neoproterozoic stromatolitic fossil (*Tekesia* sp. and *Tungussia* sp.) at the bottom of the Tianshuihai Group. The Phanerozoic sedimentary rocks (Cambrian Tianshuihu Group, Lower Silurian Wenquangou group and Triassic Bayankala Group) are in fault contact with the Precambrian metamorphic rocks (Fig. 2). The Tianshuihai Group comprises mainly a suite of greenschist-facies metamorphosed, shallow-marine siliciclastic rocks and sedimentary carbonates, including strongly deformed chloritoid phyllite, schistose argillite, chlorite calc-schist, metasandstone, marble and dolomite (Li et al., 2008). The Cambrian Tianshuihu Group includes carbonaceous slate and siltstones, together with foliated fine-grained dolomite and limestone (Li et al., 2008). The Lower Silurian Wenquangou Group consists of siliciclastic rocks and sedimentary carbonates, with small amounts of andesitic volcanic rocks. The Triassic Bayankala Group is composed of medium-thick, metamorphosed arkose, intercalated with quartz siltstone and slate. There are four major faults in the region, among which the NW–SE trending Kangxiwa and Hongshanhu–Qiaoertianshan crustal-scale faults (Fig. 1b) have exerted significant controls on the orientation and distribution of the stratigraphy and magmatic rocks. Locally, a series of linear tight folds are developed.

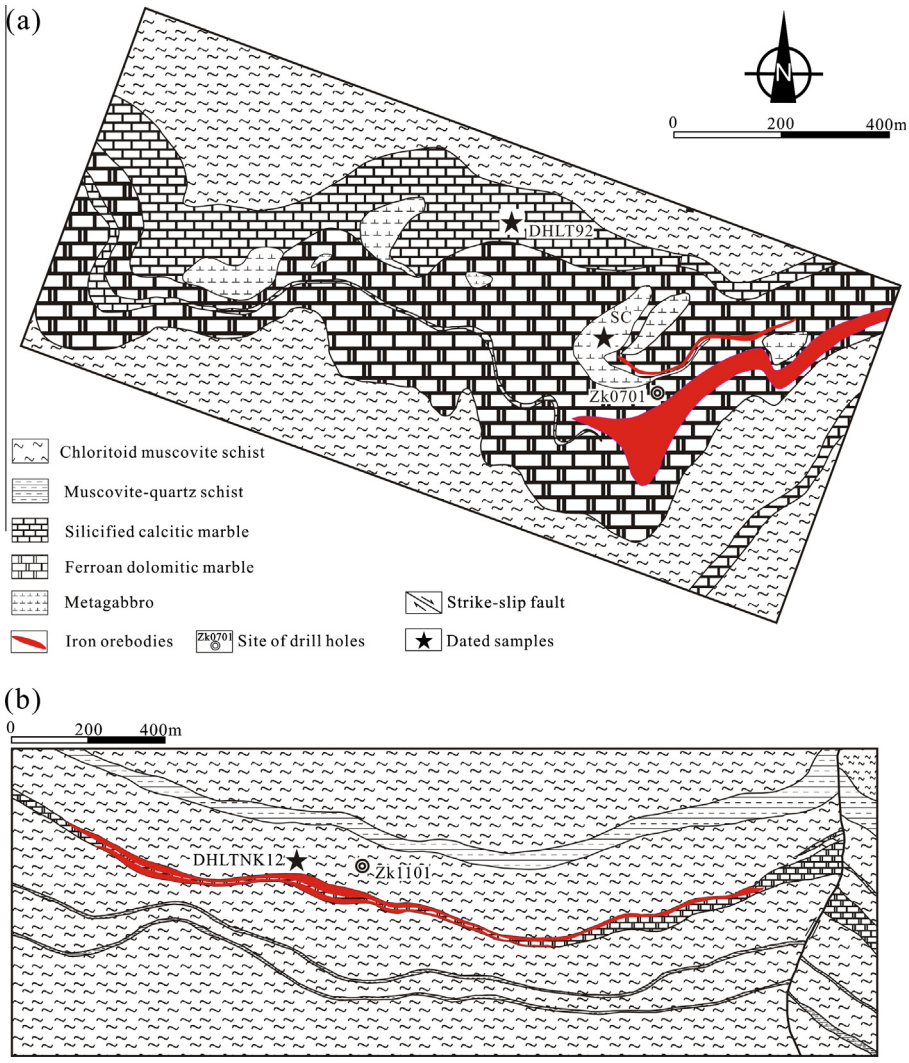

Fig. 4. Geological map of the typical Fe orebodies and locations of drill holes. (a) Fe1 orebody, and (b) Fe7 orebody, showing ore morphologies with strong folding and spatial relationship between Fe orebodies and strata at Dahongliutan.

Igneous rocks in this region mainly comprise small batholiths and stocks of granites, granodiorites and diorites (Fig. 2). Ages of these granitoids range from Neoproterozoic to Mesozoic (855–187 Ma) (Pan, 1996; Zhang and Xie, 1989; Jiang et al., 2002, 2013; Bian et al., 2013; Chen et al., 2013; Huang, 2014; Liu et al., 2015). Regional metamorphism is widespread, and dynamic metamorphism mainly occurred along fault zones. Contact metamorphism, characterized by andalusite schists, occurred mainly in the center of the mine district where biotite-quartz monzonite intruded into the Tianshuihai Group.

3. Ore deposit geology

3.1. Host rocks

The Dahongliutan Fe deposit is hosted by the metamorphosed siliciclastic rocks and sedimentary carbonates of the Tianshuihai Group (Fig. 2). The host rocks consist of ferroan dolomitic marble, silicified calcitic marble, chloritoid–muscovite schist and muscovite–quartz schist (Figs. 3, 4a and b and 5a and b), which are in some places intercalated with quartzites, garnet-muscovite–quartz schist and biotite-plagioclase–quartz schist. The strata are overall monoclinic, and strike 310–25°, with middle to steep dipping at 36–81°.

Among the aforementioned lithologies, the most significant is the ferroan dolomitic marble, the main host rock of the Fe-ores. The rock outcrops area ranges from 0.06 to 0.62 km^2 (Fig. 3). Mineralogically, ferroan dolomitic marble is made up of ankerite, dolomite, quartz, calcite, and minor hematite, limonite, siderite and muscovite. The rock is characterized by medium to fine grained granoblastic textures (Fig. 6d), as well as massive, schistose and banded structures. The massive ferroan dolomitic marble (with granoblastic textures) contains anhedral ankerite and quartz, euhedral dolomite and lepidoblastic–granoblastic hematite (Fig. 6d). The banded ferroan dolomitic marble (Fig. 5c–c5) consists of alternating white to off-white dolomite, ankerite and red hematite. The rock often occurs as a transitional zone between the silicified marble/schist and the Fe-rich ore beds (Fig. 5c–c1).

Other important rock types are silicified calcitic marble, chloritoid–muscovite schist and muscovite–quartz schist. The silicified calcitic marble area is generally 0.02–0.46 km^2 (Fig. 3) and the rock outcrops intercalated with schists and orebodies (Fig. 4a) locally thinning or pinching. Silicified calcitic marble consists of calcite, quartz and subordinate muscovite and is texturally and structurally similar to the ferroan dolomitic marble. In the massive silicified

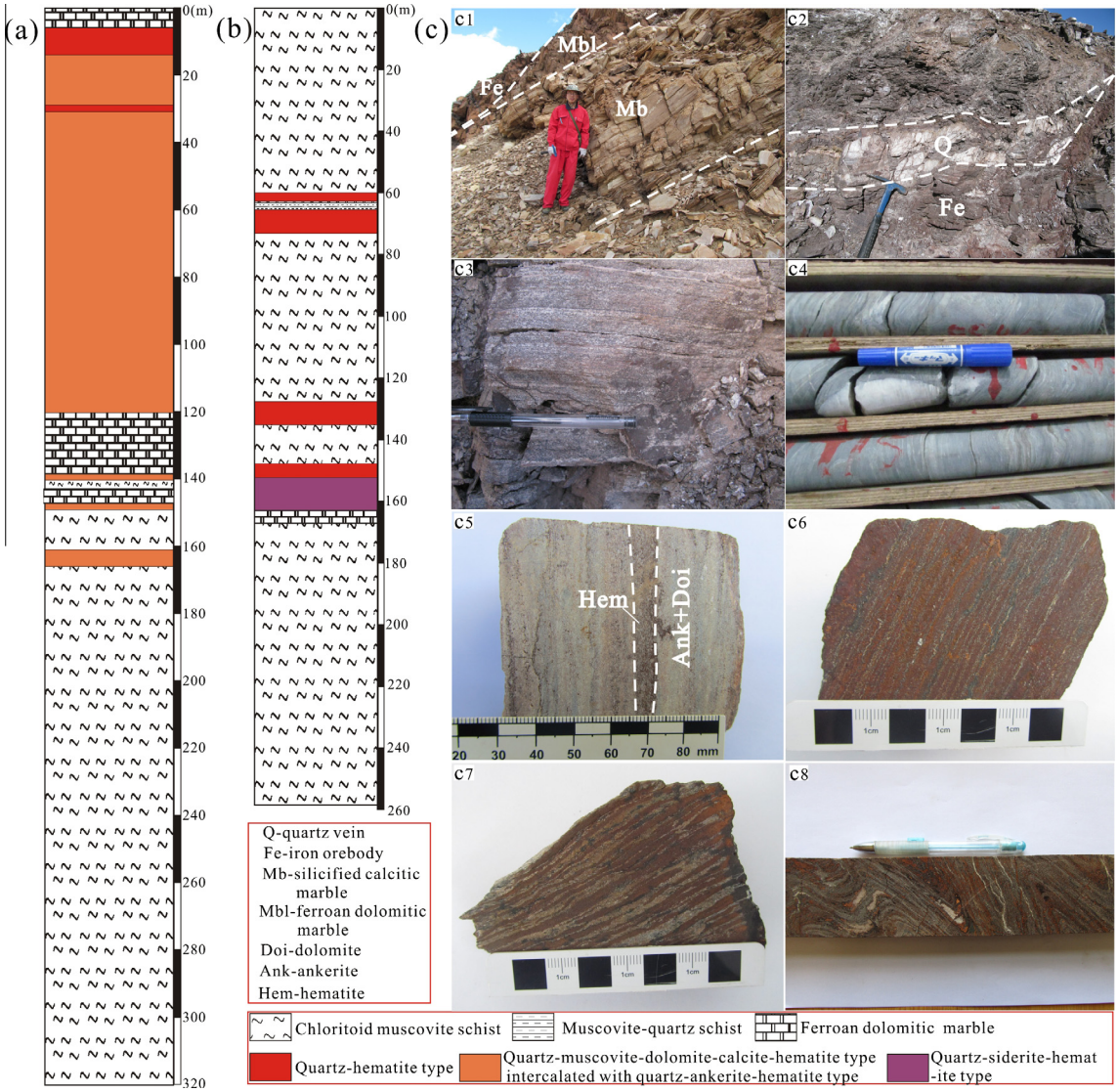

Fig. 5. The diagrams associated with drill holes (a) Zk0701 and (b) Zk1101. (c) Field and drill core photographs. (c): (c1) Fe orebodies interlayered with ferroan dolomitic marbles; (c2) Filled quartz veins in the Fe orebody; (c3) Type 4 ore, showing alternating quartz-rich (light color) and siderite- and hematite rich (brown-red) bands; (c4) Banded chloritoid muscovite schist with folding; (c5) Typical banded ferroan dolomitic marble, hand specimen; (c6) Drill core sample of typical type 1 ore showing alternating mm- to cm-scale hematite-rich and quartz-rich banding; (c7) Type 2 ore with mesobands of Fe minerals and gangue minerals; (c8) Drill core sample of banded type 3 ore showing strong "S-type" folding. (For interpretation of the references to color in this figure legend, the reader is referred to the web version of this article.)

calcitic marble, quartz and calcite are present as anhedral granoblastic aggregates. The banded silicified calcitic marble is composed of alternating gray quartz–muscovite bands with white to off-white calcite bands (Fig. 6c). Chloritoid–muscovite schist is the main rock type, approximately E–W in the mining area (Fig. 4a and b). The rock is strongly foliated, locally with strong deformation (Fig. 5c–c4). Major minerals of the schists include quartz, muscovite and chloritoid (Fig. 6a), with subordinate plagioclase and sericite (muscovite) and minor carbon. Muscovite–quartz schist comprises quartz and muscovite, with subordinate biotite and pennine, locally with carbon, dolomite and calcite (Fig. 6b). The rock outcrops usually interbedded with chloritoid–muscovite schist (Fig. 4b). The schists display lepidoblastic–granoblastic (Fig. 6a), nematoblastic and rotary textures, and phyllitic, schistose and banded structures (Fig. 5c–c4).

3.2. Ore-controlling structures

There are widespread small-scale folds, foliation and joints, accompanying ductile or brittle deformation, together with secondary NS or NW trending small-scale faults (Figs. 3 and 4b). These occur with the development of felsic mylonites and fractures trending 330–150° and dip angle ranging from 65° to 82° in the wall rocks. Most of the Fe orebodies show a clear conformable contact with the wall rocks, along the NW–SE trending tectonic line (Figs. 3 and 4b). Locally, the occurrence and morphology of the iron orebodies are controlled by the complex fold structures (Fig. 4a). These Fe orebodies are complex with "palm" and "meandering" shape. The Fe orebodies in the northwestern section of the mining area are the most complicated layer with increased thickness (Fig. 4a). In addition, some small-scale Fe orebodies have a close contact with the quartz veins in-filling interstratified fractures (Fig. 5c–c2).

3.3. Intrusive rocks

Magmatic rocks in the mining district are mainly composed of gray medium-grained porphyritic biotite-quartz monzonite, with subordinate yellowish pink-gray medium to fine grained biotite-quartz monzonite and gray-green metagabbro (albite–actinolite

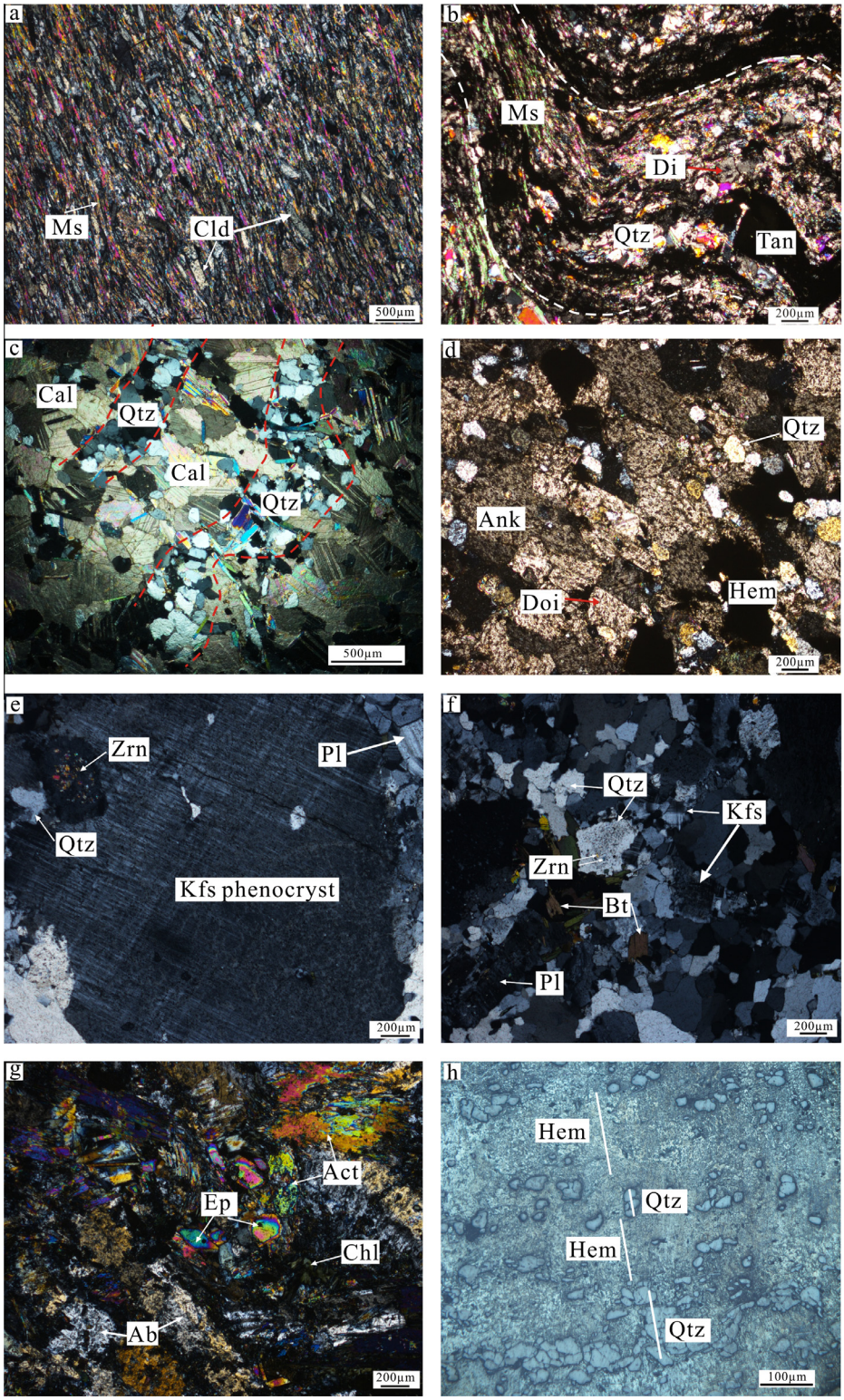

Fig. 6. Photomicrographs of various rock types at Dahongliutan. (a) Chloritoid–muscovite schist displaying lepidoblastic textures (Crossed polar); (b) Highly folded muscovite–quartz schist (Crossed polar); (c) Typical banded silicified calcitic marble (Crossed polar); (d) Massive ferroan dolomitic marble with granoblastic textures (Crossed polar); (e) Porphyritic biotite adamellites (Crossed polar); (f) Medium to fine grained biotite adamellites (Crossed polar); (g) Metagabbro displaying nematoblastic texture (Crossed polar); (h) Microbanding type 1 ore (Reflected Light). Ms = muscovite, Cld = chloritoid, Qtz = quartz, Doi = dolomite, Tan = carbon, Cal = calcite, Ank = ankerite, Hem = hematite, Pl = plagioclase, Kfs = K-feldspar, Bt = biotite, Zrn = zircon, Ab = albite, Act = actinolite, Ep = epidote, Chl = chlorite.

schist) (Figs. 3 and 4a). The biotite-quartz monzonite stocks are mainly exposed to the south of the mine, whereas minor metagabbro to the north.

The porphyritic biotite-quartz monzonite contains quartz (35–40%), plagioclase (30–35%), K-feldspar (28–30%), and biotite (5%) with accessory minerals (<5%) including zircon, apatite and

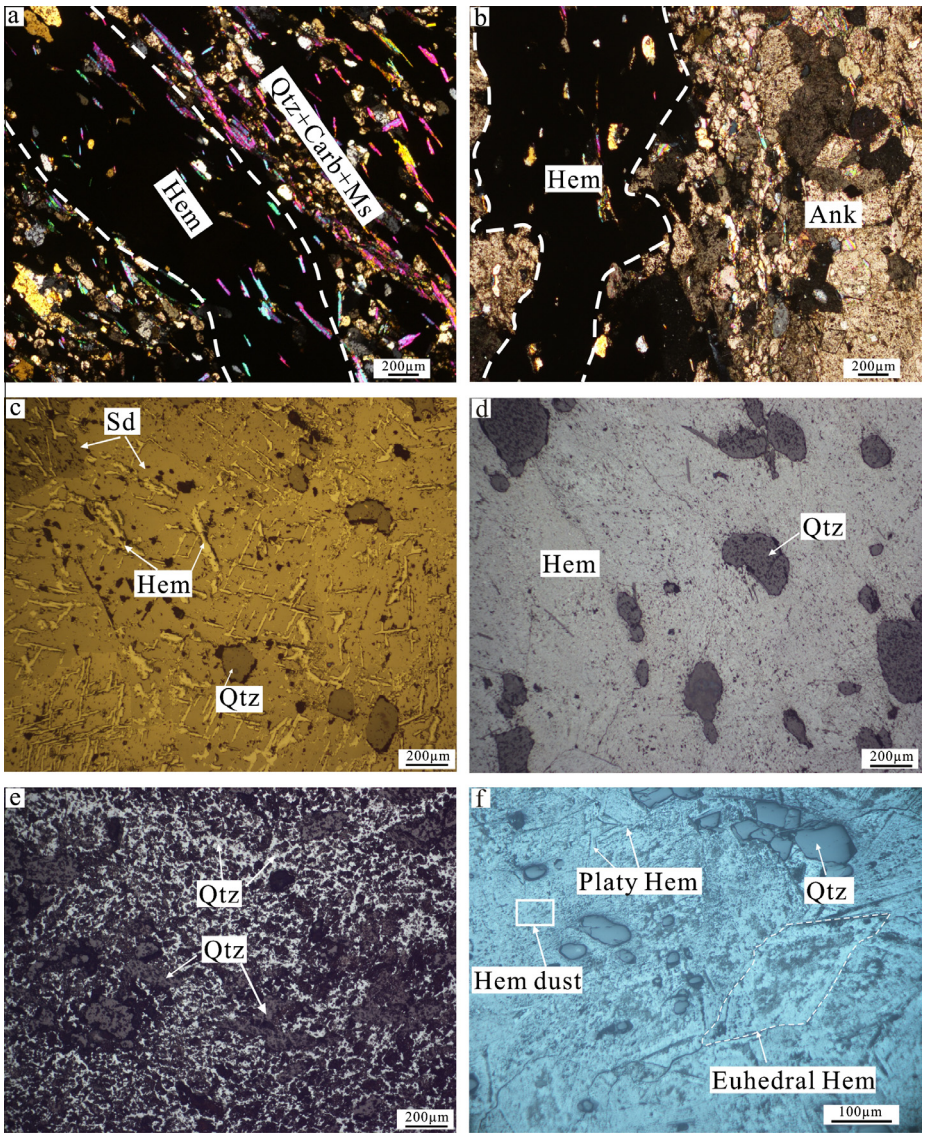

Fig. 7. Photomicrographs illustrating various textures of Fe ores at Dahongliutan. (a) Type 2 ore composed of alternating hematite-rich and quartz–carbonate–muscovite microbands, reflected light; (b) Microbanded type 3 ore, reflected light; (c) Metasomatic texture in type 4 ore, reflected light; (d) Blastopsammitic texture in type 1 ore, reflected light; (e) Type 1 ore exhibiting lepidoblastic texture, reflected light; (f) Hematite dust, platy hematite, euhedral hematite and anhedral quartz in massive type 1 ore. Qtz = quartz, Carb = carbonate, Ms = muscovite, Hem = hematite, Ank = ankerite, Sd = siderite.

magnetite. Also, the porphyritic biotite-quartz monzonite contains phenocrysts (>5 mm) of subhedral plagioclase and K-feldspar (Fig. 6e). The medium to fine-grained (0.2–2 mm) biotite-quartz monzonites contain quartz (32–38%), plagioclase (28–33%), K-feldspar (32–38%), and biotite (5%) with some accessory minerals (<5%) including zircon, apatite and magnetite (Fig. 6f). Metagabbro is composed of albite (40–45%), actinolite (40–45%), epidote (8–12%) and chlorite (5%) (Fig. 6g), and have granoblastic–nematoblastic texture, massive and slight gneissosity structure. A few actinolite grains exhibit slight chloritization.

3.4. Metamorphism

The Dahongliutan Fe deposit was subjected to regional metamorphism, dynamic metamorphism and contact metasomatism. Greenschist facies regional metamorphism led to the development of schists and quartzites. Metamorphic minerals include mainly quartz, muscovite, chloritoid, albite, actinolite and chlorite. The dynamic metamorphism is represented by mylonitic and ductile deformation. Contact metasomatism corresponds to magnesian–calcic skarn, producing mineral assemblages that include diopside, epidote and garnet, in the contact zone of granites, metagabbros and marbles.

3.5. Ore texture and structure

The Dahongliutan Fe-ore deposit contains tens orebodies of various scales, which are divided into the northern- and southern belts (Fig. 3). The northern belt is 5 km long, with width ranging from 20 to 150 m. The southern belt is 12 km long, with width of 2–32 m (Fig. 2). The two belts have trend largely to NW, with dip to N or NE at an angle of 36–70° (Fig. 2). The deposit contains Fe (t) grade ranging from 18 to 53 wt.% (average 35 wt.%).

The Fe orebodies present laminate, stratoid and lenticular, mainly interlayered with ferroan dolomitic marbles in the field (Figs. 3 and 4a). Nevertheless, in drill holes (especially the southern Belt), the marble strata are pinching-out locally in the deep part, and the orebodies are interlayered with schists (Fig. 5b). A few orebodies occur in the schists or along the marble–schist contact zone (Fig. 4b). The majority of orebodies are parallel to the strata. The

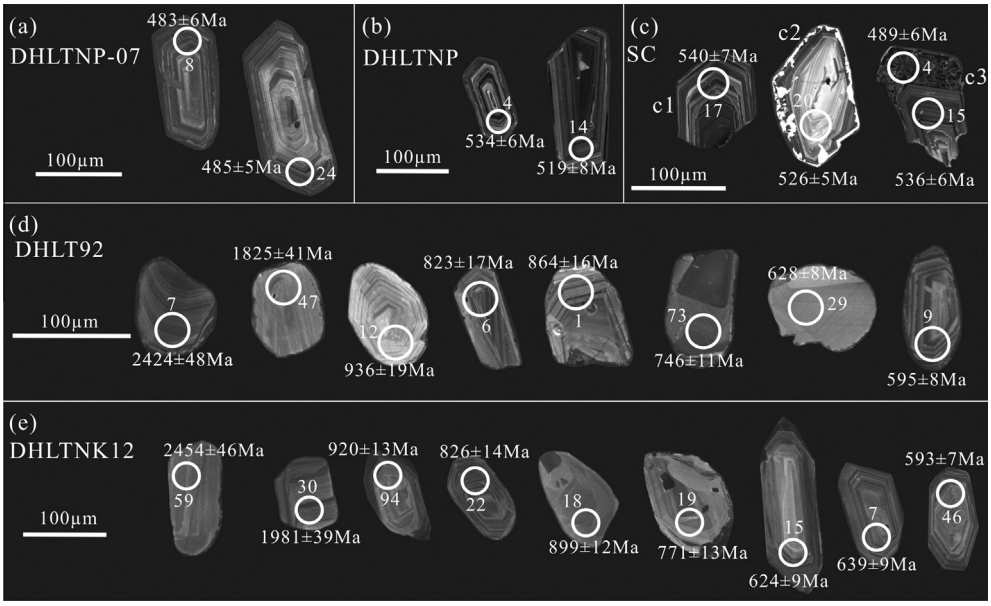

Fig. 8. Representative zircon CL images from both the intrusive rocks and meta-siliciclastic–carbonate rocks at Dahongliutan. White circles show laser spots.

orebodies trend tens to hundreds of meters length (locally up to 2000 m) with 2–150 m thickness, and locally extend for more than 100 m depth (Figs. 3 and 5a).

Ore minerals are mainly hematite with minor siderite, limonite, chalcopyrite and chalcocite. Gangue minerals include quartz, dolomite, ankerite, calcite, muscovite and chloritoid, with subordinate feldspar, and carbon. The ores display lepidoblastic (Fig. 7e), blastopsammitic (Fig. 7d), metasomatic (Fig. 7c), colloform and crystalloblastic textures, and massive and banded structures (Figs. 6h and 7a–c). Macrobands are poorly developed in ores (from drill holes), whereas mesobands and microbands are better developed (Fig. 5c and c6–c8) as ore and gangue minerals form thin rhythmic layers with (0.1–30 mm widths), occasionally with strong "S-type" deformation due to squeezing effects of the ore-controlling tectonic stress, exhibiting a successive NW to NE trending transition of mineral bands (Fig. 5c–c8). At a microscopic scale, mineral grains show dusty, euhedral–anhedral and (micro)-platy textures (Fig. 7c–f).

Based on the different combination of the ore and gangue minerals, the Fe ores are sub-divided into four types:

(1) Type 1 (Quartz–hematite) ore: This is the principal ore type, and composed of 50–85% hematite, 6–55% quartz and <5% muscovite, accounting for 90% of the total ore reserves. Most Fe ores are characterized by massive structures. Mesobands are defined by alternating mm- to cm-scale, hematite-rich and quartz-rich bands (Fig. 5c–c6). Microbands, defined by alternating sub-mm- to mm-scale hematite and quartz laminations, are common (Fig. 6h). Hematite occurs in four different forms, including large euhedral, anhedral, (micro)-platy and hematite dust (Fig. 7e and f).

(2) Type 2 (Quartz–dolomite–calcite–muscovite–hematite) ore: This type comprises 25–60% hematite, 10–35% dolomite + calcite, 6–23% quartz, and 5–15% muscovite. Despite not as important as Type 1, Type 2 is present in all orebodies and mineralization zones (Fig. 5a). Mesobands and microbands defined by alternating ore and gangue minerals laminae are common (Figs. 5c–c7 and 7a).

(3) Type 3 (Quartz–ankerite–hematite) ore: This type includes 40–70% ankerite, 5–15% quartz, 6–28% hematite and 3–5% muscovite. This ore type has low Fe(t) grade and is usually interlayered with Type 2 ores and ferroan dolomitic marble (Fig. 5a). Type 3 ores shows interbedded white to off-white ankerite–quartz bands (0.5–30 mm width) and hematite bands (0.1–0.5 mm width) (Figs. 5c–c8 and 7b).

(4) Type 4 (Quartz–siderite–hematite) ore: This type is made up of 20–70% siderite, 6–18% quartz, 18–55% hematite and 1–3% muscovite. Type 4 ores are distributed mainly in the Southern Belt (Fig. 5b), and display massive or banded structures that contain alternating siderite and hematite mesobanding (1–3 cm width) (Fig. 5c–c3). Metasomatic texture is common in this ore type, showing micro-platy hematite replacement of euhedral siderite (Fig. 7c).

4. Sampling and analytical methods

For zircon U–Pb dating, five samples were collected from wall-rocks and intrusive rocks in the mining district. Samples DHLT92 (weight: ca. 5 kg) and DHLTNK12 (weight: ca. 5 kg) (Fig. 4a and b) are, respectively, silicified calcitic marble and chloritoid–muscovite schist interbedded with the Fe orebodies. Samples DHLTNP-7 (weight: ca. 2 kg) (Fig. 2), DHLTNP (weight: ca. 2 kg) (Fig. 2) and SC (weight: ca. 10 kg) (Fig. 4a) are, respectively, medium-grained porphyritic biotite-quartz monzonite, medium-fined grained biotite-quartz monzonite, and metagabbro.

Zircon grains were separated from crushed the aforementioned samples in a steel jaw crusher using heavy liquids and magnetic techniques and then handpicked under a binocular microscope. The grains were then mounted in epoxy.

The internal structures of zircons were studied with cathodoluminescence (CL) imaging using a JXA-8100 Electron Probe Microanalyzer with a Mono CL3 Cathodoluminescence System for high resolution imaging and spectroscopy at the Guangzhou Institute of Geochemistry (GIG), Chinese Academy of Sciences. The CL images were also used to identify appropriate sites for in-situ isotopic analyses.

Zircon U–Pb dating and trace element analysis were performed using LA-ICP-MS in the State Key Laboratory of Isotope Geochemistry, GIG. A pulsed Resonetic 193 nm ArF excimer laser with laser energy of 80 mJ, a repetition rate of 8 Hz and a spot diameter of 31 μm was used in connection with an Agilent 7500a ICP-MS by Hegas via a Squid system. Data were acquired for 31 s with the

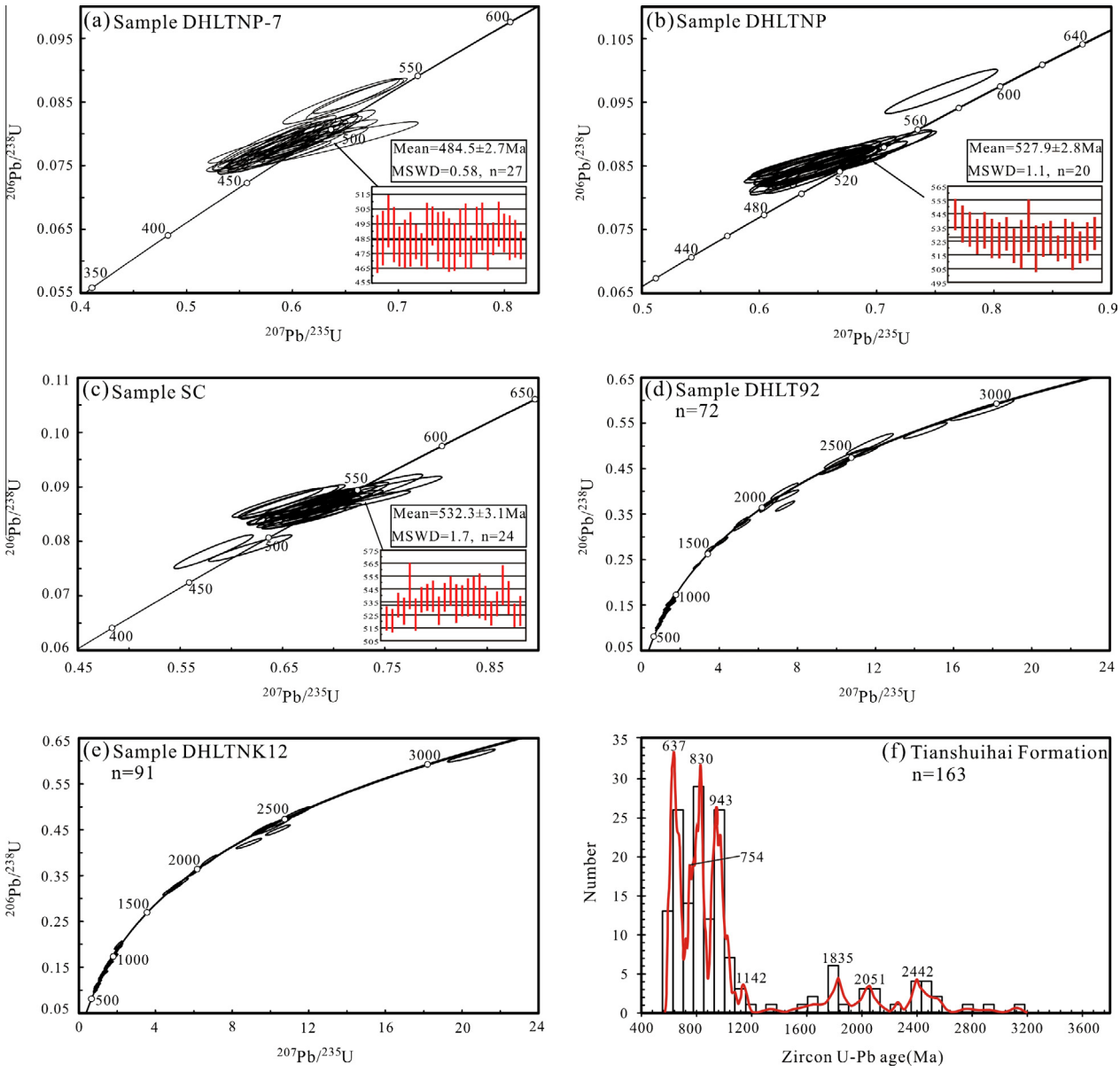

Fig. 9. Zircon U–Pb ages diagrams.

laser off. NIST610 and TEM were used as an external calibration standard, and ^{29}Si as the internal standard. The calculations of zircon isotope ratios and zircon trace elements were performed by ICPMSDataCal (Liu et al., 2008). The age calculation and plotting of concordia diagrams was performed using Isoplot/Ex 3.0 (Ludwig, 2003). Analytical results are presented in the Appendix (Tables 1–3).

5. Zircon U–Pb dating results

5.1. Intrusive rocks

5.1.1. Medium-grained porphyritic biotite-quartz monzonite

Zircons from sample DHLTNP-7 are prismatic, euhedral and transparent. They are 40–220 μm long and 20–100 μm wide (Fig. 8a). In the CL images, the zircons exhibit clear concentric oscillatory zoning that is consistent with a magmatic origin (Belousova et al., 2002) (Fig. 8a).

In addition, the Th/U ratios and REE patterns of zircons have been commonly used to assess their origins (Maas et al., 1992; Ma et al., 2012b). Generally, magmatic zircons have high Th/U ratios (>0.4), whereas metamorphic zircons have low Th/U ratios (<0.1) (Corfu et al., 2003). However, it is difficult to distinguish between igneous and metamorphic origins with only Th/U ratios. Magmatic zircons are enriched in heavy REE (HREE) compared to light REE (LREE), with steep-rising REE patterns, and show a distinctive positive Ce anomaly as well as negative Eu anomalies. By contrast, metamorphic zircons show marked depletion of HREE, characterized by flat MREE–HREE patterns without negative Eu or Ce anomaly (Maas et al., 1992; Belousova et al., 1998, 2002; Hoskin and Ireland, 2000; Rubatto, 2002; Corfu et al., 2003; Hoskin and Schaltegger, 2003; Whitehouse and Platt, 2003; Yao et al., 2011; Ma et al., 2012b).

Variations in Ce and Eu anomalies have also been used to interpret specific crystallization conditions of zircons. Anomalous abundances of Ce or Eu, usually both, are a feature of all igneous zircon

(Hoskin and Schaltegger, 2003; Ma et al., 2012b). Schreiber et al. (1980) proposed that the magnitude of the Ce-anomaly will be governed by the abundance of Ce^{4+} in the melt and this is related to the Ce^{4+}/Ce^{3+} ratio which is a function of oxygen fugacity. Europium may exist in magmas as both a divalent and trivalent cation. The Eu-anomaly in zircon is both inherited from the Eu-depleted melt (plagioclase fractionation) as well as being influenced by fO_2 (Hoskin et al., 2000; Hoskin and Schaltegger, 2003).

The zircons from sample DHLTNP-7 have high Th/U ratios (0.30–0.51) (Appendix Table 1) and display remarkable positive Ce anomalies, negative Eu anomalies, HREE enrichment relative to LREE (Fig. 10a), suggesting a magmatic origin. Twenty-seven grains yielded $^{206}Pb/^{238}U$ ages ranging from 476 to 497 Ma (Table 1), with a weighted mean age of 484.5 ± 2.7 Ma (MSWD = 0.58) (Fig. 9a). The mean age is considered to be the time of granite emplacement. In addition, three inherited zircons yielded $^{206}Pb/^{238}U$ ages of 532, 528 and 526 Ma (Fig. 9a), revealing older magmatic event.

5.1.2. Medium-fine grained biotite-quartz monzonite

Zircons from the biotite-quartz monzonite sample DHLTNP are prismatic, euhedral and transparent. The zircons have length of 60–240 μm with width of 20–180 μm. In CL images, the zircon grains show clear concentric oscillatory zoning (Fig. 8b) and have high Th/U ratios (0.35–0.55) (Appendix Table 1), indicating a magmatic origin. Moreover, the REE patterns of the zircon grains are typical of magmatic zircons (Fig. 10b). Twenty grains yielded $^{206}Pb/^{238}U$ ages ranging from 519 to 544 Ma (Appendix Table 1), with a weighted mean age of 527.9 ± 2.8 Ma (MSWD = 1.1) (Fig. 9b). The latter can be interpreted as the emplacement age of the granite. In addition, one inherited zircon yielded a $^{206}Pb/^{238}U$ age of 595 Ma (Fig. 9b).

5.1.3. Metagabbro

Almost all the zircons from the metagabbro (sample SC) are prismatic, euhedral and transparent. They are 50–160 μm long and 30–105 μm wide. Based on CL images, zircon domains in sample SC can be grouped into three types. Type 1 zircons, which are the main zircons type, exhibit distinct oscillatory zoning (Fig. 8c–c1). Type 2 zircons display clear oscillatory zoning and narrow growth rims (Fig. 8c–c2). Type 3 zircons have the cores with well-preserved concentric oscillatory zoning and structureless rims (Fig. 8c–c3). Twenty-four analyses including Type 1 zircons and the cores of Type 2 and Type 3 zircons show high Th/U ratios between 0.34 and 0.54 (Appendix Table 1), indicating a magmatic origin. The analyses yielded $^{206}Pb/^{238}U$ ages ranging from 521 to 548 Ma (Appendix Table 1) with a weighted mean age of 532.3 ± 3.1 Ma (MSWD = 1.7) (Fig. 9c). This mean age is interpreted as reflecting the time of the gabbro emplacement. Additionally, two analyses (SC-4 and SC-25) (Appendix Table 1) from the rims of Type 3 zircons yielded $^{206}Pb/^{238}U$ ages of 485 ± 8 and 489 ± 6 Ma, respectively.

5.2. Silicified calcitic marble and chloritoid–muscovite–quartz schist (Tianshuihai formation)

Eighty-one and ninety-eight analyses were obtained from sample DHLT92 (a silicified calcitic marble) and sample DHLTNK12 (a chloritoid–muscovite–quartz schist), respectively (Appendix Table 2). Among the 179 zircon analyses from the two samples, 163 analyses have <10% discordance (Appendix Table 2). The remaining 16 analyses with >10% discordance are excluded in the following discussion. For statistical purposes, $^{206}Pb/^{238}U$ ages are used for grains <1200 Ma, and $^{207}Pb/^{206}Pb$ ages are used for grains >1200 Ma (Yang et al., 2012).

Most of the detrital zircons are euhedral to subhedral, suggesting a near-source region; some of the zircon grains are rounded or sub-rounded in morphology, indicating that they have experienced long-distance transportation or abrasion. In addition, some grains are fragmented with sharp edges (Fig. 8d, e). In CL-images, the majority of the zircons display oscillatory zoning (incl. sector zoning) (Fig. 8d and e). These zircons show high Th/U ratios (0.13–2.82) (Appendix Table 2), pronounced positive Ce anomalies, negative Eu anomalies and steep-rising REE patterns (Fig. 10d), which are typical of igneous origin. A few zircon grains exhibit no zoning, or contain narrow rims with inherited cores (Fig. 8d and e), relatively low Th/U ratios (0.07–0.66) (Appendix Table 2), flat REE patterns and weak or no positive Ce anomalies (Fig. 10d), which suggest a metamorphic origin.

The detrital zircon grains from samples DHLT92 and DHLTNK12 (less than ±10% discordant) yielded a wide range of ages from 3122 to 593 Ma (Fig. 9d–f). The data seem to fall in six major age populations, namely 2561–2329, 2076–1644, 1164–899, 869–722 and 696–593 Ma, with prominent peaks at ca. 943, 830, 754 and 637 Ma, as well as minor peaks at ca. 2442, 2051, 1835 and 1142 Ma (Fig. 9f).

The youngest zircon grains yielded ages of 595 ± 8 and 593 ± 7 Ma from samples DHLT92 and DHLTNK12, respectively. Our studies also obtained Mesoarchean components as represented by zircons with age values of 2909 ± 64 and 3122 ± 40 Ma (Fig. 9d and e) from samples DHLT92 and DHLTNK12, respectively.

6. Discussion

6.1. Provenance and depositional age and of the meta-siliciclastic–carbonate rocks at Dahongliutan

Age spectra of detrital zircons have been successfully employed to derive information on provenance characteristics in many recent studies (Condie et al., 2009; Rino et al., 2008; Yao et al., 2011). The age distribution of detrital zircon grains from the meta-siliciclastic–carbonate rocks at Dahongliutan clearly demonstrates that the grains crystallized between Mesoarchean to Neoproterozoic (3122–593 Ma), implying multiple sources and a variety of rocks in the provenance.

The existence of the ca. 2561–2328 Ma zircon age population (peak: ca. 2442 Ma) in our samples is an important finding. Similar Archean–Paleoproterozoic ages have been reported from the high-grade metamorphic- and volcanic rocks in the North Kunlun and Tianshuihai terranes.

For instance, Yuan et al. (2002), Zhang et al. (2003b), Wang (2008, 2011) and Ji et al. (2011) have reported ages of 2481 ± 14 Ma (metavolcanic rocks), 2426 ± 12 Ma (gneissic granite), 2210–2270 Ma (hornblende plagiogneiss) and 2130–2700 Ma (schists and gneisses). Therefore, the Paleoproterozoic rocks in either the North Kunlun or the Tianshuihai terranes, or both of them, are likely the detrital sources for the Tianshuihai metasedimentary rocks.Regarding the zircon age population of 2076–1644 Ma (small peaks: ca. 2051 and 1835 Ma), a few metamorphic ages of 1900 ± 12 Ma (gneissic granite) (Zhang et al., 2003c, 2007) and 2016 ± 39 Ma (meta-volcanic rocks) (Ji et al., 2011) have been reported in the North Kunlun and Tianshuihai terranes. The 2000–1830 Ma metamorphic event have been widely recognized in the North Kunlun terrane (Wang, 2011). On the other hand, the detrital zircons with age peaks of ca. 2051 and 1835 Ma in our study are mainly euhedral to subhedral with oscillatory zoning (incl. sector zoning), so they were likely derived from a nearby source. Thus, we infer that the detrital zircons with ages in the range of 2076–1644 Ma might have been derived mainly from the North Kunlun and Tianshuihai terranes.

Our data also show a Late Mesoproterozoic–Early Neoproterozoic age population ranging between ca.1164 and 899 Ma (major peak: 943 Ma; minor peak: 1142 Ma). Zhang et al. (2003a) reported

two Ar–Ar ages of 1050.85 ± 0.93 and 1021 ± 1.08 Ma from volcanic rocks in the North Kunlun terrane. The 0.9–1.0 Ga metamorphic event have been widely recognized in the North Kunlun terrane (Zhang et al., 2003a, 2007). Magmatic events with ages ranging from 1000 to 890 Ma in the Tarim Block have also been reported (Zhang et al., 2009; Shu et al., 2011; Ma et al., 2012a,b). Therefore, we conclude that the Northern Kunlun terrane, and probably also the Tarim Block, may have been the sources for the ca. 0.94 and 1.1 Ga detrital zircons.

The major zircon age population of 869–722 Ma (peaks: ca. 830 and 754 Ma) is also considered to be tectonically important for the Western Kunlun orogenic belt. Zhang et al. (2007) and Wang (2008) reported a 0.8 Ga metamorphic event and the ca. 850 Ma basalt in the North Kunlun and Tianshuihai terranes. Besides, zircon ages of 815 ± 57, 836 ± 12 and 855 ± 14 Ma have been obtained for the gneissic granite and tonalite from the Northern Kunlun and Tianshuihai terranes (Zhang et al., 2003d; Bian et al., 2013). Neoproterozoic dolerite and basalt (820–600 Ma) in the Northern Kunlun terrane have also been reported (Li et al., 2008; Zhang et al., 2009). Moreover, detrital zircons with age peaks at ca. 840 and 800 Ma were identified in the Northern Kunlun terranes (Wang, 2011). Thus, we consider that the 869–722 Ma detrital zircons at Dahongliutan may have been derived from the Northern Kunlun and Tianshuihai terranes.

A prominent age peak at 637 Ma (Fig. 9f) for the 696–593 Ma age population in our U–Pb age spectra deserves special attention. The direct evidence for synchronous magmatic rocks or contemporaneous metamorphic or deformational events have not yet been found in the Tianshuihai terrane, the Late Neoproterozoic–Cambrian ages obtained in our study suggest the existence of a provenance from which these zircons were sourced. Detrital zircon age peaks of 690, 625, 620 and 618 Ma have been reported in the Tarim-, Qiangtang-, Lhasa-, and Himalaya blocks (Dong et al., 2011; He et al., 2011;

Ravikant et al., 2011; Zhu et al., 2011a,b; He et al., 2014). Also, the 660–610 Ma magmatic rocks, including the potassic granitoids (Ge et al., 2012), peraluminous granite (Luo et al., 2011) and mafic dykes (Zhu et al., 2008, 2011a,b) in the northern Tarim Craton, have been reported. The timing of the metamorphism at ca. 650 Ma was obtained for the granulites in the Lhasa terrane (Zhang et al., 2012a,b). In addition, most zircons are euhedral (Fig. 8d and e), indicating a nearby detrital source. Only several zircons are sub-rounded or rounded, which likely represent long-distance transportation or abrasion. Because exposures of the rocks of these ages are currently unknown in the region, a possible interpretation is that the source rocks were either deeply buried, or have been eroded or reworked.

To summarize, provenance studies show that detritals of the metamorphosed siliciclastic and sedimentary carbonate rocks from the Neoproterozoic Tianshuihai Group were mainly sourced from the North Kunlun and Tianshuihai terranes.

The age of the youngest detrital zircon grain can be used to constrain the maximum depositional age (Yang et al., 2012; Babinski et al., 2013). The youngest age among the detrital zircons from the metamorphosed siliciclastic and sedimentary carbonate rocks at Dahongliutan is 593 ± 7 Ma, and this Neoproterozoic detrital zircon is euhedral with well-developed oscillatory zoning (Fig. 8e), and a relatively high Th/U ratio (0.98), a positive Ce anomaly, and a negative Eu anomaly (Fig. 10d), indicating a magmatic origin. Sedimentary rocks associated with the Dahongliutan Fe-ore deposit experienced greenschist facies metamorphism, which also precludes the possibility that the U–Th–Pb systems in the detrital zircons have been reset. In addition, the inherited zircon with an age of 595 Ma from the medium to fine grained biotite-quartz monzonite also reflect a similar Precambrian crustal source. Therefore, we regard 593 Ma as the maximum depositional age for the metasediments.

6.2. Age of the Dahongliutan Fe deposit

The Fe-ore bodies in the Dahongliutan deposit are interlayered with marbles and schists. Therefore, the maximum depositional age of the metamorphosed siliciclastic–carbonate rocks can constrain the ore-forming age of the deposit.U–Pb dating result indicates that the Dahongliutan quartz monzonite and metagabbro intrusion occurred during the Cambrian–Early Ordovician (i.e., 484.5 ± 2.7, 527.9 ± 2.8 and 532.3 ± 3.1 Ma), providing a younger age constraint for the metamorphosed siliciclastic–carbonate rocks in the mine. Thus, we constrain the Dahongliutan Fe deposit formation age to be ca. 532–593 Ma.

Although REE patterns (Fig. 10c) of the zircon rims, with ages of 485 ± 8 and 489 ± 6 Ma from metagabbro are compatible with a metamorphic origin, Liou et al. (1974) proposed that the upper boundary for the greenschist assemblage albite–chorite–epidote–actinolite is 475 °C. At that temperature, greenschist-facies rocks normally do not contain significant metamorphic zircons. However, the boundaries of the zircon rims are even and parallel to that of the zircon cores (Fig. 8c–c3), likely indicating the recrystallization of the former zircons due to the effect of fluid (metamorphic or hydrothermal fluids) (Hoskin and Black, 2000; Geisler et al., 2001; Hoskin and Schaltegger, 2003). The metamorphic fluids in the Dahongliutan mining district may result from regional metamorphism and contact metasomatism related to the metagabbros and marbles. In addition, the two ages are coeval with the emplacement age (484.5 ± 2.7 Ma) of the medium-grained porphyritic biotite-quartz monzonite. Moreover, Chen et al. (2013), Huang (2014), Yan et al. (2012) and Zhang et al. (2007) identified the 463–530 Ma regional metamorphic events at Taxkorgan in the western part of the Tianshuihai terrane. Thus, the two ages of zircon rims from metagabbro likely represent a response to late magmatic or metamorphic events. We infer a regional metamorphic event may have occurred at ca. 480 Ma.

6.3. Comparison with typical BIF deposits in the world

Banded Iron Formations (BIFs), typically thin bedded or laminated, are chemical sediments containing >15 wt.% Fe_2O_3 and composed of intercalated microcrystalline quartz, iron oxides, iron-rich silicates and carbonates (James, 1954; Pickard, 2003; Basta et al., 2011; Cox et al., 2013). The deposition of BIFs requires an anoxic water column to transport ferrous iron to sites of iron precipitation. Their formation was episodic (Rasmussen et al., 2012). Deposition of BIFs began at 3.8 Ga (Isua, West Greenland) (Klein, 2005). The majority of BIFs were deposited between 2.7 and 2.45 Ga (before the rise of atmospheric oxygen by 2.32 Ga), and BIFs deposition largely disappeared from the geological record at ca. 1.8 Ga (Klein, 2005; Rasmussen et al., 2012). After a billion year hiatus, BIFs reappeared in the Neoproterozoic between 0.85 and 0.6 Ga (Klein, 2005; Ilyin, 2009; Bekker et al., 2010; Xu et al., 2014). Based on the differences in formation ages, depositional environments, host rocks and mineral assemblages, Precambrian BIFs are divided into Algoma-, Superior- and Rapitan-types (Gross and Mcleod, 1980; Huston and Logan, 2004; Klein, 2005; Bekker et al., 2010, 2012; Basta et al., 2011; Li et al., 2014; Xu et al., 2014). Algoma-type BIFs occur along volcanic arcs, rift zones or deep-seated fault and fracture systems in deep oceans (Goodwin, 1962; Basta et al., 2011; Li et al., 2014; Xu et al., 2014), are relatively small and associated with coeval volcanic suites. Most of Algoma-type BIFs were developed in the Neoarchean and Paleoproterozoic periods (3.0–1.8 Ga), such as BIFs in the greenstone belts of Abitibi in Canada, Yilgarn in Australia, Dharwar in southern India, and North China

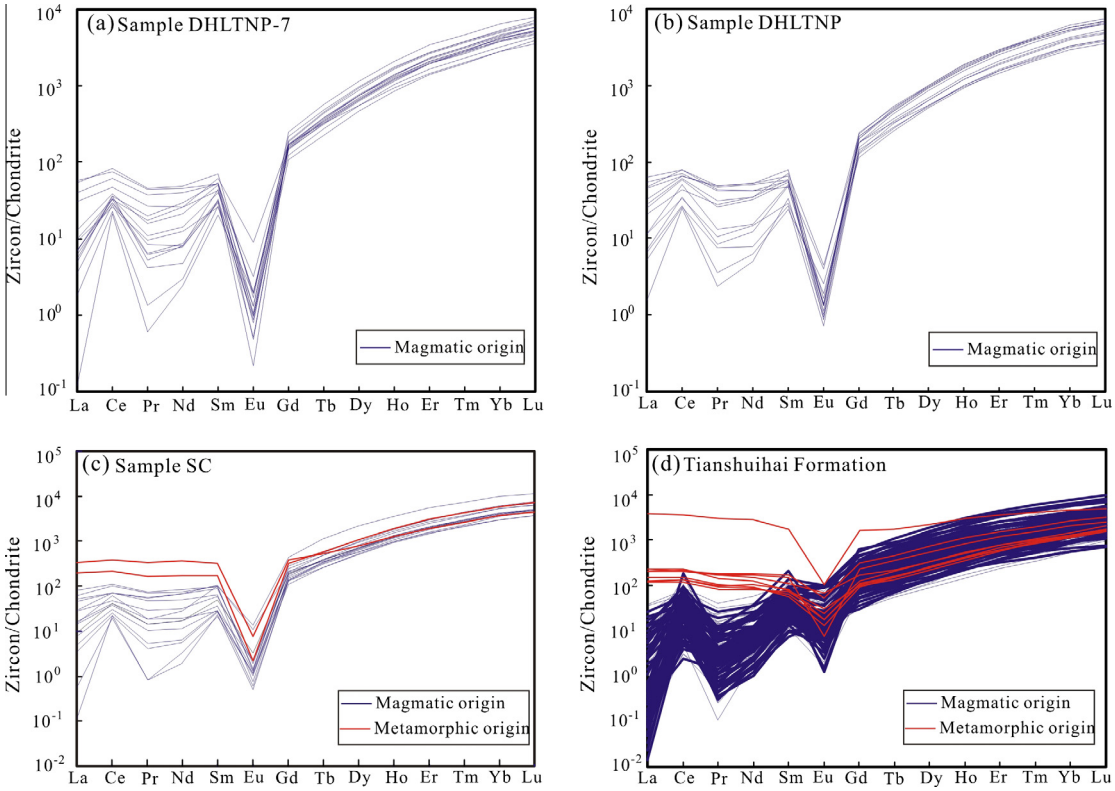

Fig. 10. Chondrite-normalized REE patterns of zircons. Chondrite REE values are after Sun and McDonough (1989).

Craton in China (Klein and Beukes, 1992; Huston and Logan, 2004; Klein, 2005; Zhang et al., 2011, 2012a,b; Li et al., 2014). Some BIFs in greenstone belts are considered to be a hydrothermal–metasomatic origin and occur along sheared lithological contacts, such as bedding and/or foliation truncation (Alexandrov, 1973; Hofmann et al., 2003). Sheared contacts between basalt and shale seem to be the most common site of ironstone formation, with shale being the host rock of the ironstone (Hofmann et al., 2003). A few Neoproterozoic (750–660 Ma) Fe deposits, which are intimately related to volcanic activity accompanying the breakup of Rodinia, formed in the Arabian-Nubian Shield (ANS) basin were also classified as Algoma-type, indicating that the recurrence of anoxic ferruginous deep sea and Neoproterozoic Oxidation Event in the Cryogenian and Ediacaran (Basta et al., 2011; Khalil and El-Shazly, 2012; Stern et al., 2013). Superior-type BIFs are generally large and mostly related to sedimentary formations (e.g., quartzite, dolomite, black shales), in transgressive sequences on shallow continental shelves with no volcanic association. Superior-type BIFs were mainly formed in the Paleoproterozoic (2.5–1.8 Ga), with examples including the Hamersley in Australia, Quadrilatero Ferrifero in Brazil, Lake Superior in North America, Kursk in Russia, Transvaal in South Africa, Yuanjiacun-type iron deposits (in the Shanxi province), and Dalizi-type iron deposits(in Jilin province) (Klein and Beukes, 1989, 1992; Zhai and Windley, 1990; Sun et al., 1998; Klein and Ladeira, 2000; Spier et al., 2003, 2007; Klein, 2005; Hayashi et al., 2007; Li et al., 2014). In addition, the Neoproterozoic Jingtieshan-type iron deposit (in Gansu province) in China is considered as a Superior-type BIF (Sun et al., 1998). Xu et al. (2013, 2014) also reported that the Neoproterozoic (830–960 Ma) Shilu Fe deposit in the western Hainan Province of south China belong to Superior-type BIF. The Rapitan-type BIFs are associated with Neoproterozoic glaciogenic sequences (diamictites, conglomerates, quartzites and siltstones) and may be linked to Snowball Earth conditions (Lottermoser and Ashley, 2000; Hoffman and Schrag, 2002; Klein and Ladeira, 2004; Halverson et al., 2011) or glaciated rift environment (Young, 2002). Rapitan-type BIFs have been widely reported to be related to the prominent Neoproterozoic glacial events (Sturian: 718–660 Ma; Marinoan: 651–635 Ma), such as those in the Rapitan in Canada, Urucum in Brazil, the Adelaide Geosyncline in South Australia, Damara in South Africa, southern Paraguay Belt in Brazil and Jiangnan paleocontinent in South China Block (Tang et al., 1987; Klein and Beukes, 1993; Lottermoser and Ashley, 2000; Klein and Ladeira, 2004; Ilyin, 2009; Babinski et al., 2013; Cox et al., 2013; Li et al., 2014).

In addition, Archean and Paleoproterozoic BIFs minerals contain mainly quartz, magnetite, hematite, amphibole, pyroxene, stilpnomelane, minnesotaite, chlorite, minor siderite, dolomite–ankerite and rare detrital minerals. The macrobands, mesobands (<2.54 cm) and microbands (0.3–1.7 mm) are usually well preserved, although low-grade greenschist-metagabbro facies metamorphism occurred in most Fe deposits (Trendall and Blockley, 1970; Klein, 2005). In most Neoproterozoic BIFs, iron resides almost exclusively in hematite (Klein and Beukes, 1993; Cox et al., 2013) instead of magnetite (Volkert et al., 2010; Freitas et al., 2011). Accessory minerals include chlorite, quartz and carbonate. Manganese is also a significant component of Neoproterozoic BIFs. Detrital material inputs are common, and bands are poorly developed or entirely absent in most Neoproterozoic BIFs (Cox et al., 2013).

We have summarized the basic geological characteristics of the Dahongliutan Fe deposit to compare with typical BIFs in the world: (1) The Dahongliutan Fe deposit developed between ca. 532 and 593 Ma. The host rocks are a suite of shallow marine siliciclastic and sedimentary carbonate rocks subjected to greenschist-facies metamorphism, without volcanic rocks. (2) The length and outcrop area of the Fe mineralization zones are, respectively, above 15 km and 400 km^2, with proven ore reserves over 100 Mt. The Fe orebodies are laminate, quasi laminate and lenticular in form, mainly interlayered with ferroan dolomitic marbles and schists, and

strata-controlled. (3) Ore minerals are mainly hematite, minor siderite and limonite, with rare sulfides, whereas gangue minerals include quartz, dolomite, ankerite, calcite, muscovite and chloritoid. (4) Macrobands are poorly developed, mesobands and microbands are well preserved as alternating ore and gangue mineral laminates (0.1–30 mm). (5) Hematitic dust indicates sedimentary texture that does not show any replacement texture (Stern et al., 2013), and likely represents some of the earliest components of BIFs. If they did form very early, then the precursor phase probably was a form of ferric oxyhydroxide, such as ferrihydrite (Bekker et al., 2014). The local preservation of blastopsammitic and microcrystalline Fe ores also provide good support for a sedimentary origin (Xu et al., 2013). (6) Greenschist facies regional metamorphism is conspicuous, mineral orientations (Fig. 6a), strongly folded foliation (Fig. 6b) in the schists and a transition from phyllitic and schistose rocks with lepido-granoblastic textures to banded rocks and laminated rocks (Fig. 5c–c4). (7) Aluminosilicates (muscovite, chloritoid, etc.) in the Fe ores are considered to be as the result of the incorporation of a detrital component.

Combined with U–Pb dating result, the geological characteristics of the Dahongliutan Fe deposit is consistent with that of the major Neoproterozoic BIFs. In comparison with typical BIF deposits in the world, the Dahongliutan district contains no evidence of contemporaneous volcanic rocks. Consequently, either the seafloor volcanic exhalative model or the hydrothermal vent model related to mantle plumes or hot spots would require the BIFs being intercalated with tholeiitic basalts (e.g., Algoma-type BIFs) (Adekoya, 1998; Bekker et al., 2010; Basta et al., 2011; Khalil and El-Shazly, 2012; Rasmussen et al., 2012), which is clearly not the case at Dahongliutan. On the other hand, the Dahongliutan BIF seems comparable to the Neoproterozoic Rapitan-type BIFs. For example, the Neoproterozoic (ca.750–700 Ma) BIFs in the eastern part of the Adelaide Geosyncline of South Australia comprises abundant Fe oxides (hematite, magnetite) and quartz, minor silicates (muscovite, chlorite, biotite, plagioclase, tourmaline), carbonate and apatite, and detrital mineral grains and lithic clasts, and was subjected to greenschist facies (biotite grade) metamorphism (Lottermoser and Ashley, 2000). However, the Dahongliutan BIF contains no evidence of contemporaneous glacimarine sedimentary rocks (e.g., tillites and diamictites). Because the Tianshuihai Group host rocks are a dominantly submarine siliciclastic and carbonate sedimentary succession, two principal possibilities exist, namely the hydrogeneous-sedimentary processes (Holland, 1973; James and Sims, 1973) and the hydrothermal exhalative processes (Gross, 1991; Kimberley, 1989), which have been proposed for the origin of and very large accumulations of Fe in the Superior-type BIFs, could be considered to interpret the formation of the Dahongliutan BIF. For example, the host rocks, mineral assemblages, and ore texture and structure of the Dahongliutan BIF suggest a resemblance to Paleoproterozoic BIFs at Quadrilatero Ferrifero in Brazil, which are hosted in shallow marine siliciclastic–carbonate sediments (dolomite and phyllite) (Spier et al., 2003, 2007) and Early Proterozoic Fe-formations (among carbonates and shales) developed in the Transvaal Supergroup in South Africa (Klein and Beukes, 1989).

The Neoproterozoic or temporally similar hematite-rich BIF-type deposits in China have been reported in the Jingtieshan, Gansu Province of North China (Sun et al., 1998) and in the western Hainan Province of south China (Xu et al., 2013, 2014). The Jingtieshan deposit in North China, which is hosted by a suite of rift-type marine sediments of the Neoproterozoic Jingtieshan Formation comprising fine-grained clastic sedimentary rocks, carbonate rocks with a small amount of andesitic basalts, is characterized by the upper Fe orebodies dominated by specularite and jasper with lesser amounts of magnetite, hematite, siderite, and barite, and the lower Cu orebodies composed of pyrite and chalcopyrite occurring as disseminated and stockwork mineralization (Sun et al., 1998; Xu et al., 2014). Sun et al. (1998) and Li et al. (2014) suggested that the Jingtieshan deposit, which is a sedimentary exhalative origin, belongs to Superior-type. However, the Jingtieshan deposit contains typical banded jasper–barite–iron formation and stratabound Cu mineralization beneath the iron formation, which do not occur in the Dahongliutan BIF. The Neoproterozoic Shilu iron formation in South China, which is hosted within a suit of submarine siliciclastic and carbonate sedimentary succession subjected to greenschist-facies metamorphism, consists of Fe-rich ores dominated by hematite (~85%), locally with minor magnetite (⩽1%), quartz (~14%), anhydrite and barite (~1%), Fe-poor ores (or amphibolitic itabirites) comprising hematite (20–40%), magnetite (20–45%), garnet (20–25%), quartz (~19%), feldspar(~5%), diopside and actinolite (~4%) and barite (~1%), as well as minor titanite and biotite, and Co–Cu ores including cobaltiferous pyrite, cobaltiferous pyrrhotite, chalcopyrite, quartz sericite, dolomite and calcite (Xu et al., 2009, 2013, 2014). Xu et al. (2013, 2014) proposed that the Shilu Fe-ore deposit, which formed under anoxic but Fe^{2+}-rich conditions, belongs to Lake Superior-type BIF and Fe and Cu–Co orebodies precipitated possibly from sea floor hydrothermal fluids which likely were associated with the break-up of the Rodinian supercontinent due to mantle superplume activity in South China. This genetic model seems feasible for the Dahongliutan BIF. However, it is not compatible with all the characteristic features including the dominant pyroxene–amphibole rocks, amphibolitic itabirites and the Fe–Co–Cu association in the Shilu district.

Most typical BIFs do not have more than 35 wt.% Fe(t) (Klein, 2005). However, the Dahongliutan hematite-rich Fe deposit contains Fe-rich ores, which are marked by more than 50 wt.% Fe(t). Most world-class high-grade Fe ore deposits are the product of epigenetic enrichment of Precambrian BIFs (Gutzmer et al., 2006). For example, the high-grade (>63 wt.% Fe(t)) martite–microplaty hematite Fe ore deposits mostly hosted within BIFs in the Hamersley province of northwest Western Australia, Taylor et al. (2001), Thorne et al. (2009) and Gutzmer et al. (2006) suggested that meteoric fluids were responsible for the hydrothermal enrichment of BIFs to high grade iron ores. Hofmann et al. (2003) suggested that surface weathering gives rise to a gossaneous appearance and obliterates primary structural feature. Xu et al. (2009, 2013) also proposed the formation of Fe-rich ores in the Shilu hematite-rich ore deposit are due to the interaction meteoric fluids and the original BIF during the oxidation-leaching stage. The existence of micro-platy hematite replacement of euhedral siderite, and the occurrence of recently formed limonite as the main constituent of gossan in the Dahongliutan Fe deposit, possibly suggests that supergene oxidation and leaching by meteoric fluids were responsible for the ore upgrade.

Comparing the Dahongliutan BIF with other Fe deposits in the Tianshuihai terrane, we can learn more about the origin of the Dahongliutan BIF. Yan et al. (2012) and Huang (2014) suggest that the deposits (e.g., Zankan, Yelike, Laobing Fe deposits) are classified as sedimentary–metamorphic Fe deposits related to marine volcanism, formed in 510–530 Ma. Negative Ce anomaly, positive Eu anomaly from biotite quartz schist, plagioclase amphibole schist and Fe ores indicate that these deposits may have formed under anoxic reductive condition (Huang, 2014).

In summary, the Dahongliutan Fe-ore deposit belongs to Neoproterozoic (Ediacaran) BIF-related sedimentary metamorphic type iron deposit. In comparison with Superior-type BIF, the Dahongliutan BIF exhibits similarity in host rocks, mineral assemblages, and banded compositions and structures. The Dahongliutan BIF may represent a case for the reappearance of iron formation during the Neoproterozoic, which reflecting the recurrence of anoxic ferruginous conditions in the Neoproterozoic–Early Cambrian deep sea (Isley and Abbott, 1999; Kump and Seyfried,

2005; Canfield et al., 2007, 2008; Johnston et al., 2010, 2012; Basta et al., 2011; Shields and Och, 2011; Cox et al., 2013).

7. Conclusion

1. The Dahongliutan Fe deposit is mainly hosted within the Neoproterozoic Tianshuihai Group neritic siliciclastic–carbonate rocks subjected to greenschist-facies metamorphism. Most orebodies are laminated–quasi laminated interlayered with ferroan dolomitic marbles and schists. Mineral assemblage contains hematite, siderite, limonite, quartz, dolomite, ankerite, calcite, muscovite and chloritoid. Banded and massive structures dominate the Fe ores, which generally show lepidoblastic, crystalloblastic and blastopsammitic textures. We have divided the ores into four types, namely: (1) Quartz–hematite; (2) Quartz–dolomite–calcite–muscovite–hematite; (3) Quartz–ankerite–hematite; (4) Quartz–siderite–hematite.
2. Zircon U–Pb analyses on the marbles and schists yielded a Neoproterozoic age (Ediacaran; 593 ± 7 Ma), whereas those on the ore-intruding medium-grained porphyritic biotite-quartz monzonite, medium to fine grained biotite-quartz monzonite and metagabbro yielded Cambrian–Early Ordovician ages (i.e., 484.5 ± 2.7, 527.9 ± 2.8 and 532.3 ± 3.1 Ma), which altogether constrain the ore formation to the Late Neoproterozoic to Early Cambrian (532–593 Ma).
3. The 163 detrital zircon ages from marbles and schists define five major age populations: 2561–2329 Ma (a peak of 2442 Ma), 2076–1644 Ma (two peaks at 2051 and 1835 Ma), 1164–899 Ma (a major peak at 943 Ma and a subordinate peak at 1142 Ma), 869–722 Ma (a major peak of 830 Ma and a subordinate peak of 754 Ma) and 696–593 Ma (a prominent peak of 637 Ma). Provenance studies show that detritals of the sediments at Dahongliutan were mainly sourced from the North Kunlun and Tianshuihai terranes.
4. Comparing the Dahongliutan Fe deposit with typical BIF deposits in the world, we infer that the deposit belongs to Neoproterozoic (Ediacaran) BIF-related sedimentary metamorphic type iron deposit and appears similar to Superior-type BIF, probably reflecting the recurrence of anoxic ferruginous conditions in the Neoproterozoic–Early Cambrian deep sea.

Acknowledgements

This study is financially supported by the State Technology Support Program (2011BA06B05-01) and the GIGCAS 135 project of the Guangzhou Institute of Geochemistry (Y234021001). The authors appreciate Hongwei Han and Yong Wei from the Xinjiang Xindi Geological Exploration Company for their logistic supports during the field work. We are indebted to Profs. Deru Xu and Hecai Niu for their fruitful discussions that enable the completion of this paper. We are also grateful to Profs. Yusheng Wan, Xianglin Tu and Yuquan Zhang for their help in the LA-ICP-MS zircon U–Pb and REE analyses. Cenozoic Geoscience Editing is acknowledged for their language polishing and scientific editing services. Special thanks are due to Profs. J.G. Liou, Andery Bekker and Wenjiao Xiao for carefully reviewing the manuscript and for their constructive comments.

Appendix A

See Tables 1–3.

Table 1
U–Pb dating results on zircons from intrusive rocks at the Dahongliutan Fe deposit.

Spots	Isotopic ratios						Apparent age (Ma)				Th	U	Th/U	Con.
	$^{207}Pb/^{206}Pb$	1σ	$^{207}Pb/^{235}U$	1σ	$^{206}Pb/^{238}U$	1σ	$^{207}Pb/^{235}U$	1σ	$^{206}Pb/^{238}U$	1σ	(ppm)			
Sample DHLTNP-7: Gray medium-grained porphyritic biotite-quartz monzonite														
DHLTNP-7-1	0.05371	0.00150	0.57693	0.01898	0.07756	0.00163	462	12	482	10	704	1764	0.40	95
DHLTNP-7-2	0.05373	0.00150	0.58439	0.01903	0.07819	0.00153	467	12	485	9	528	1229	0.43	96
DHLTNP-7-3	0.05579	0.00200	0.61992	0.02387	0.08011	0.00147	490	15	497	9	396	927	0.43	98
DHLTNP-7-4	0.05507	0.00141	0.60241	0.01812	0.07860	0.00155	479	11	488	9	524	1367	0.38	98
DHLTNP-7-5	0.05307	0.00135	0.57536	0.01566	0.07726	0.00112	461	10	480	7	919	2484	0.37	96
DHLTNP-7-6	0.05214	0.00148	0.56899	0.01780	0.07755	0.00136	457	12	481	8	588	1675	0.35	94
DHLTNP-7-7	0.05186	0.00157	0.57129	0.01916	0.07807	0.00153	459	12	485	9	515	1326	0.39	94
DHLTNP-7-8	0.05133	0.00172	0.56599	0.01857	0.07778	0.00097	455	12	483	6	771	2496	0.31	94
DHLTNP-7-9	0.05276	0.00194	0.57947	0.02039	0.07691	0.00092	464	13	478	5	778	2306	0.34	97
DHLTNP-7-10	0.05344	0.00197	0.60080	0.02519	0.07844	0.00187	478	16	487	11	474	1208	0.39	98
DHLTNP-7-11	0.05478	0.00227	0.62050	0.02457	0.07956	0.00110	490	15	494	7	248	563	0.44	99
DHLTNP-7-12	0.05356	0.00222	0.59860	0.02421	0.07836	0.00138	476	15	486	8	634	1932	0.33	97
DHLTNP-7-13	0.05504	0.00295	0.61901	0.04090	0.07799	0.00161	489	26	484	10	1104	2659	0.42	98
DHLTNP-7-14	0.05455	0.00273	0.60050	0.02906	0.07742	0.00151	478	18	481	9	493	1140	0.43	99
DHLTNP-7-15	0.05425	0.00220	0.59011	0.02407	0.07721	0.00134	471	15	479	8	744	1872	0.40	98
DHLTNP-7-16	0.05359	0.00210	0.59640	0.02306	0.07880	0.00135	475	15	489	8	269	694	0.39	97
DHLTNP-7-17	0.05460	0.00217	0.60111	0.02486	0.07843	0.00184	478	16	487	11	484	1178	0.41	98
DHLTNP-7-18	0.05502	0.00205	0.64608	0.02257	0.08510	0.00146	506	14	526	9	434	1003	0.43	96
DHLTNP-7-19	0.05563	0.00165	0.59433	0.01732	0.07664	0.00091	474	11	476	5	545	1821	0.30	99
DHLTNP-7-20	0.05541	0.00140	0.66384	0.01818	0.08597	0.00114	517	11	532	7	471	1170	0.40	97
DHLTNP-7-21	0.05552	0.00180	0.59964	0.01683	0.07910	0.00131	477	11	491	8	568	1111	0.51	97
DHLTNP-7-22	0.05681	0.00174	0.62078	0.01852	0.07951	0.00134	490	12	493	8	443	1248	0.36	99
DHLTNP-7-23	0.05770	0.00412	0.58664	0.01600	0.07721	0.00132	469	10	479	8	1008	2357	0.43	97
DHLTNP-7-24	0.05411	0.00144	0.58817	0.01500	0.07813	0.00092	470	10	485	5	548	1560	0.35	96
DHLTNP-7-25	0.05394	0.00142	0.60012	0.01682	0.07978	0.00127	477	11	495	8	479	1098	0.44	96
DHLTNP-7-26	0.05608	0.00132	0.61390	0.01500	0.07879	0.00109	486	9	489	6	969	1953	0.50	99
DHLTNP-7-27	0.05633	0.00140	0.60830	0.01497	0.07826	0.00124	482	9	486	7	509	1476	0.35	99
DHLTNP-7-28	0.05613	0.00146	0.60627	0.01535	0.07814	0.00106	481	10	485	6	443	1162	0.38	99
DHLTNP-7-29	0.05491	0.00121	0.59000	0.01330	0.07739	0.00078	471	8	481	5	1071	2525	0.42	97

(*continued on next page*)

Table 1 (*continued*)

Spots	Isotopic ratios						Apparent age (Ma)				Th	U	Th/U	Con.
	$^{207}Pb/^{206}Pb$	1σ	$^{207}Pb/^{235}U$	1σ	$^{206}Pb/^{238}U$	1σ	$^{207}Pb/^{235}U$	1σ	$^{206}Pb/^{238}U$	1σ	(ppm)			
DHLTNP-7-30	0.05567	0.00146	0.65913	0.01882	0.08541	0.00129	514	12	528	8	256	713	0.36	97
Sample DHLTNP: Pink-gray medium-fine grained biotite-quartz monzonite														
DHLTNP-1	0.05631	0.00129	0.75512	0.01963	0.09671	0.00142	571	11	595	8	445	969	0.46	95
DHLTNP-2	0.05816	0.00115	0.71177	0.01610	0.08812	0.00096	546	10	544	6	686	1820	0.38	99
DHLTNP-3	0.05619	0.00132	0.67558	0.01692	0.08694	0.00112	524	10	537	7	387	867	0.45	97
DHLTNP-4	0.05736	0.00120	0.68719	0.01605	0.08631	0.00106	531	10	534	6	1046	1887	0.55	99
DHLTNP-5	0.05596	0.00129	0.66128	0.01546	0.08542	0.00107	515	9	528	6	521	1239	0.42	97
DHLTNP-6	0.05489	0.00151	0.65831	0.01864	0.08617	0.00112	514	11	533	7	413	1065	0.39	96
DHLTNP-7	0.05493	0.00163	0.65103	0.01899	0.08519	0.00119	509	12	527	7	312	827	0.38	96
DHLTNP-8	0.05367	0.00200	0.64283	0.02267	0.08499	0.00109	504	14	526	7	338	765	0.44	95
DHLTNP-9	0.05341	0.00167	0.64482	0.02028	0.08576	0.00102	505	13	530	6	707	1729	0.41	95
DHLTNP-10	0.05558	0.00199	0.65319	0.02267	0.08430	0.00104	510	14	522	6	309	834	0.37	97
DHLTNP-11	0.05492	0.00179	0.64894	0.02324	0.08447	0.00148	508	14	523	9	896	2216	0.40	97
DHLTNP-12	0.05680	0.00170	0.68920	0.02377	0.08672	0.00160	532	14	536	10	755	1934	0.39	99
DHLTNP-13	0.05450	0.00152	0.64029	0.01949	0.08391	0.00141	502	12	519	8	808	1978	0.41	96
DHLTNP-14	0.05405	0.00154	0.64075	0.01821	0.08498	0.00101	503	11	526	6	1316	2752	0.48	95
DHLTNP-15	0.05369	0.00176	0.64114	0.02056	0.08529	0.00101	503	13	528	6	527	1467	0.36	95
DHLTNP-16	0.05478	0.00178	0.64553	0.02029	0.08396	0.00078	506	13	520	5	504	1026	0.49	97
DHLTNP-17	0.05519	0.00159	0.65953	0.01956	0.08517	0.00121	514	12	527	7	864	2053	0.42	97
DHLTNP-18	0.05578	0.00179	0.65369	0.01994	0.08427	0.00147	511	12	522	9	485	1392	0.35	97
DHLTNP-19	0.05482	0.00154	0.64998	0.01848	0.08409	0.00097	508	11	520	6	841	2094	0.40	97
DHLTNP-20	0.05472	0.00168	0.65270	0.02022	0.08482	0.00118	510	12	525	7	507	1232	0.41	97
DHLTNP-21	0.05310	0.00168	0.64188	0.01959	0.08582	0.00100	503	12	531	6	736	1566	0.47	94
Sample SC: Metagabbro														
SC-1	0.05641	0.00145	0.66475	0.01639	0.08439	0.00077	518	10	522	5	766	1882	0.41	99
SC-2	0.05711	0.00139	0.67130	0.01631	0.08410	0.00076	522	10	521	4	864	1897	0.46	99
SC-3	0.05636	0.00137	0.67737	0.01627	0.08612	0.00079	525	10	533	5	1044	1935	0.54	98
SC-4	0.05661	0.00155	0.61808	0.01663	0.07877	0.00100	489	10	489	6	430	1021	0.42	99
SC-5	0.05622	0.00183	0.66731	0.02141	0.08534	0.00088	519	13	528	5	291	667	0.44	98
SC-6	0.05852	0.00196	0.72189	0.02635	0.08862	0.00151	552	16	547	9	349	760	0.46	99
SC-7	0.05739	0.00158	0.67537	0.01869	0.08488	0.00105	524	11	525	6	582	1634	0.36	99
SC-8	0.05732	0.00150	0.69219	0.01851	0.08682	0.00082	534	11	537	5	840	1899	0.44	99
SC-9	0.05950	0.00169	0.72190	0.02144	0.08712	0.00087	552	13	539	5	446	826	0.54	97
SC-10	0.05603	0.00151	0.67762	0.01897	0.08728	0.00101	525	11	539	6	911	2048	0.44	97
SC-11	0.05633	0.00169	0.66552	0.02037	0.08539	0.00091	518	12	528	5	507	1277	0.40	98
SC-12	0.05744	0.00170	0.69465	0.02181	0.08713	0.00092	536	13	539	5	577	1223	0.47	99
SC-13	0.05715	0.00151	0.69576	0.01913	0.08793	0.00096	536	11	543	6	721	1604	0.45	98
SC-14	0.05653	0.00166	0.67386	0.02055	0.08631	0.00125	523	12	534	7	497	1186	0.42	97
SC-15	0.05662	0.00160	0.67969	0.02001	0.08668	0.00100	527	12	536	6	1047	2089	0.50	98
SC-16	0.05401	0.00156	0.65622	0.01959	0.08712	0.00123	512	12	538	7	628	1527	0.41	95
SC-17	0.05334	0.00175	0.65848	0.02146	0.08735	0.00125	514	13	540	7	547	1496	0.37	95
SC-18	0.05746	0.00155	0.70134	0.02124	0.08732	0.00145	540	13	540	9	514	1269	0.40	99
SC-19	0.05600	0.00133	0.67369	0.01673	0.08639	0.00110	523	10	534	7	1026	2142	0.48	97
SC-20	0.05791	0.00137	0.68695	0.01623	0.08505	0.00078	531	10	526	5	760	1922	0.40	99
SC-21	0.05709	0.00136	0.68710	0.01617	0.08628	0.00080	531	10	533	5	556	1402	0.40	99
SC-22	0.05929	0.00225	0.73379	0.02924	0.08873	0.00129	559	17	548	8	537	1137	0.47	98
SC-23	0.05315	0.00145	0.64466	0.01816	0.08709	0.00108	505	11	538	6	340	808	0.42	93
SC-24	0.05354	0.00125	0.58217	0.01577	0.07809	0.00126	466	10	485	8	875	2184	0.40	96
SC-25	0.05649	0.00134	0.66513	0.01588	0.08480	0.00075	518	10	525	4	514	1493	0.34	98
SC-26	0.05516	0.00119	0.65418	0.01571	0.08536	0.00097	511	10	528	6	777	1939	0.40	96

Table 2
U–Pb dating results for detrital zircons from meta-siliciclastic–carbonate rocks from the Tianshuihai Formation at the Dahongliutan deposit.

Spots	Isotopic ratios						Apparent age (Ma)						Th	U	Th/U	Con.
	$^{207}Pb/^{206}Pb$	1σ	$^{207}Pb/^{235}U$	1σ	$^{206}Pb/^{238}U$	1σ	$^{207}Pb/^{206}Pb$	1σ	$^{207}Pb/^{235}U$	1σ	$^{206}Pb/^{238}U$	1σ	(ppm)			
Sample DHLT92: Silicified calcitic marble																
DHLT92-1	0.06701	0.00422	1.30661	0.06330	0.14350	0.00283	839	131	849	28	864	16	160	192	0.83	98
DHLT92-2	0.06352	0.00339	1.03333	0.05441	0.11851	0.00208	726	113	721	27	722	12	143	123	1.16	99
DHLT92-3	0.06353	0.00412	1.07090	0.06785	0.12296	0.00239	728	137	739	33	748	14	143	90	1.59	98
DHLT92-4	0.06563	0.00265	1.20670	0.04991	0.13191	0.00211	794	84	804	23	799	12	182	237	0.77	99
DHLT92-5	0.07010	0.00241	1.56166	0.05527	0.15998	0.00242	931	76	955	22	957	13	263	358	0.73	99
DHLT92-6	0.06763	0.00243	1.28519	0.05319	0.13610	0.00307	857	71	839	24	823	17	608	552	1.10	98
DHLT92-7	0.15705	0.00452	10.05282	0.31086	0.45913	0.00732	2424	48	2440	29	2436	32	202	320	0.63	99
DHLT92-8	0.07004	0.00289	1.51869	0.06233	0.15676	0.00229	929	85	938	25	939	13	117	148	0.79	99
DHLT92-9	0.05934	0.00233	0.79699	0.03127	0.09670	0.00134	589	81	595	18	595	8	586	349	1.68	99
DHLT92-10	0.07007	0.00362	1.52438	0.08184	0.15611	0.00272	931	106	940	33	935	15	54	96	0.56	99
DHLT92-11	0.19206	0.00598	14.53364	0.45717	0.53430	0.00726	2761	50	2785	30	2760	30	55	416	0.13	99
DHLT92-12	0.07003	0.00459	1.48872	0.09290	0.15631	0.00340	929	134	926	38	936	19	46	64	0.72	98
DHLT92-13	0.16237	0.00695	11.68057	0.49009	0.50411	0.00941	2481	72	2579	39	2631	40	159	481	0.33	97
DHLT92-14	0.07010	0.00387	1.53801	0.08624	0.15235	0.00285	931	114	946	35	914	16	757	296	2.56	96
DHLT92-15	0.13141	0.00563	7.31250	0.29551	0.38876	0.00605	2117	75	2150	36	2117	28	150	446	0.34	98
DHLT92-16	0.21027	0.00826	17.43906	0.66029	0.57894	0.00923	2909	64	2959	36	2944	38	142	322	0.44	99
DHLT92-17	0.06334	0.00384	1.05933	0.06093	0.11899	0.00234	720	128	733	30	725	13	85	139	0.61	98
DHLT92-18	0.05978	0.00277	1.39727	0.06297	0.16513	0.00335	594	97	888	27	985	19	222	296	0.75	89
DHLT92-19	0.04839	0.00216	0.62037	0.02706	0.09056	0.00175	117	106	490	17	559	10	408	411	0.99	86
DHLT92-20	0.05801	0.00376	1.43050	0.08986	0.17534	0.00352	532	138	902	38	1041	19	94	81	1.16	85
DHLT92-21	0.05299	0.00232	0.94210	0.04041	0.12531	0.00201	328	100	674	21	761	12	401	439	0.91	87
DHLT92-22	0.13502	0.00491	5.40031	0.21415	0.28214	0.00535	2165	64	1885	34	1602	27	495	1004	0.49	83
DHLT92-23	0.06526	0.00426	1.15332	0.07429	0.12839	0.00253	783	137	779	35	779	14	81	107	0.76	99
DHLT92-24	0.15783	0.00673	10.49298	0.45893	0.47272	0.00909	2432	72	2479	41	2495	40	38	96	0.40	99
DHLT92-25	0.05740	0.00301	0.82958	0.04282	0.10276	0.00167	506	115	613	24	631	10	187	270	0.69	97
DHLT92-26	0.12842	0.00467	7.32445	0.28066	0.40006	0.00724	2076	64	2152	34	2169	33	184	178	1.04	99
DHLT92-27	0.05253	0.00227	0.84339	0.03609	0.11305	0.00198	309	131	621	20	690	11	498	467	1.07	89
DHLT92-28	0.06150	0.00301	0.87752	0.04359	0.10300	0.00152	657	110	640	24	632	9	63	100	0.63	98
DHLT92-29	0.06096	0.00247	0.85700	0.03426	0.10228	0.00137	639	89	628	19	628	8	78	106	0.73	99
DHLT92-30	0.06063	0.00179	0.84533	0.02562	0.10068	0.00113	628	63	622	14	618	7	227	221	1.03	99
DHLT92-31	0.17038	0.00343	11.51877	0.23673	0.48725	0.00455	2561	34	2566	19	2559	20	251	570	0.44	99
DHLT92-32	0.06924	0.00290	1.44841	0.06260	0.15087	0.00233	906	87	909	26	906	13	70	76	0.92	99
DHLT92-33	0.07045	0.00259	1.55337	0.05772	0.15902	0.00205	943	76	952	23	951	11	41	80	0.52	99
DHLT92-34	0.05974	0.00209	0.80475	0.02747	0.09716	0.00112	594	108	600	15	598	7	213	176	1.21	99
DHLT92-35	0.07114	0.00249	1.61232	0.05799	0.16320	0.00220	961	71	975	23	975	12	85	135	0.63	99
DHLT92-36	0.06371	0.00223	1.13334	0.03889	0.12789	0.00140	731	74	769	19	776	8	185	203	0.91	99
DHLT92-37	0.06602	0.00270	1.20778	0.04890	0.13249	0.00205	807	90	804	22	802	12	39	88	0.44	99
DHLT92-38	0.09202	0.00250	3.49560	0.09476	0.27235	0.00301	1533	51	1526	21	1553	15	229	323	0.71	98
DHLT92-39	0.08601	0.00236	2.83866	0.07797	0.23651	0.00275	1339	53	1366	21	1369	14	303	484	0.63	99
DHLT92-40	0.06214	0.00353	0.94247	0.05075	0.11006	0.00171	680	121	674	27	673	10	18	66	0.28	99
DHLT92-41	0.06709	0.00398	1.31382	0.07432	0.14397	0.00243	840	119	852	33	867	14	27	34	0.81	98
DHLT92-42	0.06954	0.00207	1.47911	0.04400	0.15278	0.00180	915	61	922	18	917	10	182	279	0.65	99
DHLT92-43	0.06185	0.00270	1.05456	0.04502	0.12433	0.00209	733	94	731	22	755	12	40	77	0.52	96
DHLT92-44	0.06794	0.00156	1.36375	0.03104	0.14440	0.00118	878	52	873	13	869	7	345	755	0.46	99
DHLT92-45	0.06012	0.00203	0.83279	0.02719	0.10041	0.00109	609	74	615	15	617	6	196	257	0.76	99
DHLT92-46	0.07063	0.00354	1.32761	0.06530	0.13674	0.00213	946	106	858	28	826	12	58	49	1.19	96
DHLT92-47	0.11157	0.00282	5.06999	0.13140	0.32775	0.00353	1825	41	1831	22	1827	17	146	206	0.71	99
DHLT92-48	0.06028	0.00292	0.83741	0.04213	0.09975	0.00145	613	106	618	23	613	8	41	83	0.50	99
DHLT92-49	0.06591	0.00236	1.21269	0.04418	0.13307	0.00185	803	74	806	20	805	11	131	180	0.73	99
DHLT92-50	0.06698	0.00339	1.25180	0.05773	0.13673	0.00202	839	106	824	26	826	11	22	173	0.13	99
DHLT92-51	0.09892	0.00610	2.30596	0.14321	0.16780	0.00285	1606	115	1214	44	1000	16	61	44	1.38	80
DHLT92-52	0.15752	0.00504	6.83454	0.23008	0.31136	0.00420	2429	55	2090	30	1747	21	227	812	0.28	82

(*continued on next page*)

Table 2 (*continued*)

Spots	Isotopic ratios						Apparent age (Ma)						Th	U	Th/U	Con.
	$^{207}Pb/^{206}Pb$	1σ	$^{207}Pb/^{235}U$	1σ	$^{206}Pb/^{238}U$	1σ	$^{207}Pb/^{206}Pb$	1σ	$^{207}Pb/^{235}U$	1σ	$^{206}Pb/^{238}U$	1σ	(ppm)			
DHLT92-53	0.05902	0.00235	0.85190	0.03359	0.10453	0.00154	569	87	626	18	641	9	185	212	0.87	97
DHLT92-54	0.06447	0.00334	1.15351	0.06114	0.12880	0.00222	767	110	779	29	781	13	71	62	1.15	99
DHLT92-55	0.07068	0.00254	1.54719	0.05558	0.15731	0.00187	948	74	949	22	942	10	207	267	0.78	99
DHLT92-56	0.06724	0.00235	1.28557	0.04418	0.13641	0.00148	856	72	839	20	824	8	700	304	2.31	98
DHLT92-57	0.06450	0.00242	1.14912	0.04378	0.12673	0.00158	767	80	777	21	769	9	113	192	0.59	99
DHLT92-58	0.06377	0.00205	1.10212	0.03441	0.12281	0.00132	744	268	754	17	747	8	467	392	1.19	98
DHLT92-59	0.15457	0.00465	9.80479	0.28307	0.44964	0.00520	2398	50	2417	27	2394	23	218	231	0.94	99
DHLT92-60	0.07012	0.00363	1.51911	0.07244	0.15644	0.00253	931	107	938	29	937	14	39	82	0.48	99
DHLT92-61	0.11131	0.00428	5.10846	0.18774	0.32558	0.00523	1821	75	1838	31	1817	25	43	107	0.40	98
DHLT92-62	0.10108	0.00285	4.11773	0.12132	0.28962	0.00392	1644	52	1658	24	1640	20	172	172	1.01	98
DHLT92-63	0.07168	0.00286	1.62418	0.06385	0.16321	0.00226	976	81	980	25	975	13	45	78	0.57	99
DHLT92-64	0.07308	0.00248	1.71519	0.05747	0.16968	0.00203	1017	69	1014	21	1010	11	108	108	1.00	99
DHLT92-65	0.07365	0.00199	1.74220	0.04780	0.17216	0.00197	1031	56	1024	18	1024	11	70	257	0.27	99
DHLT92-66	0.12459	0.00276	6.35954	0.16002	0.36933	0.00491	2033	39	2027	22	2026	23	42	602	0.07	99
DHLT92-67	0.07199	0.00201	1.63631	0.04961	0.16486	0.00244	987	57	984	19	984	13	174	319	0.55	99
DHLT92-68	0.06704	0.00215	1.27909	0.04204	0.13832	0.00157	839	67	836	19	835	9	169	277	0.61	99
DHLT92-69	0.06232	0.00284	0.89858	0.03944	0.10589	0.00151	685	103	651	21	649	9	68	132	0.51	99
DHLT92-70	0.08976	0.00277	2.26036	0.06995	0.18229	0.00177	1420	59	1200	22	1079	10	254	199	1.27	89
DHLT92-71	0.12639	0.00304	6.53326	0.19968	0.37187	0.00709	2050	47	2050	27	2038	33	875	411	2.13	99
DHLT92-72	0.11124	0.00262	5.16374	0.12908	0.33444	0.00357	1820	43	1847	21	1860	17	302	680	0.44	99
DHLT92-73	0.06519	0.00312	1.09925	0.05173	0.12270	0.00184	789	102	753	25	746	11	59	83	0.71	99
DHLT92-74	0.14353	0.00354	7.35029	0.20105	0.36749	0.00475	2270	47	2155	24	2018	22	294	742	0.40	93
DHLT92-75	0.07180	0.00235	1.64474	0.05548	0.16507	0.00213	989	67	988	21	985	12	123	180	0.69	99
DHLT92-76	0.06084	0.00237	0.88977	0.04036	0.10430	0.00139	635	85	646	22	640	8	844	416	2.03	98
DHLT92-77	0.10164	0.00309	4.08898	0.12561	0.28983	0.00368	1655	56	1652	25	1641	18	105	131	0.80	99
DHLT92-78	0.07231	0.00256	1.68071	0.05972	0.16710	0.00195	994	72	1001	23	996	11	165	191	0.87	99
DHLT92-79	0.06671	0.00332	1.25218	0.05957	0.13720	0.00194	828	104	824	27	829	11	76	71	1.06	99
DHLT92-80	0.07005	0.00283	1.47159	0.05846	0.15184	0.00168	931	78	919	24	911	9	48	113	0.43	99
DHLT92-81	0.07143	0.00287	1.57364	0.06380	0.16070	0.00260	970	81	960	25	961	14	62	92	0.67	99
Sample DHLTNK12: Chloritoid-muscovite schist																
DHLTNK12-1	0.06152	0.00306	0.91085	0.04361	0.10329	0.00152	657	107	658	23	634	9	741	263	2.82	96
DHLTNK12-2	0.05973	0.00277	0.83147	0.03900	0.09709	0.00163	594	100	614	22	597	10	313	352	0.89	97
DHLTNK12-3	0.06870	0.00266	1.57696	0.06165	0.16066	0.00329	900	80	961	24	960	18	275	375	0.73	99
DHLTNK12-4	0.14855	0.00464	8.85487	0.27206	0.42005	0.00452	2329	54	2323	28	2261	21	198	845	0.23	97
DHLTNK12-5	0.06247	0.00345	0.99779	0.05497	0.11509	0.00219	700	119	703	28	702	13	67	83	0.81	99
DHLTNK12-6	0.07376	0.00278	2.03096	0.08069	0.19790	0.00357	1035	71	1126	27	1164	19	137	258	0.53	96
DHLTNK12-7	0.06097	0.00281	0.87343	0.04097	0.10418	0.00151	639	72	637	22	639	9	131	167	0.78	99
DHLTNK12-8	0.08244	0.00327	1.58707	0.06529	0.13928	0.00192	1257	78	965	26	841	11	213	225	0.95	86
DHLTNK12-9	0.11155	0.02733	2.30756	0.61988	0.11628	0.00365	1825	458	1215	193	709	21	143	202	0.70	47
DHLTNK12-10	0.06571	0.00239	1.20326	0.04453	0.13193	0.00182	798	76	802	21	799	10	306	241	1.27	99
DHLTNK12-11	0.06113	0.00254	0.85945	0.03552	0.10178	0.00160	643	91	630	19	625	9	108	258	0.42	99
DHLTNK12-12	0.06204	0.00223	0.94283	0.03426	0.10959	0.00164	676	76	674	18	670	10	175	332	0.53	99
DHLTNK12-13	0.07428	0.00295	0.93669	0.04113	0.08927	0.00123	1050	80	671	22	551	7	491	688	0.71	80
DHLTNK12-14	0.06328	0.00247	1.00916	0.03840	0.11471	0.00156	717	83	708	19	700	9	125	384	0.33	98
DHLTNK12-15	0.06071	0.00290	0.85954	0.04010	0.10163	0.00154	628	102	630	22	624	9	68	158	0.43	99
DHLTNK12-16	0.06007	0.00299	0.86645	0.04397	0.10365	0.00167	606	107	634	24	636	10	89	186	0.48	99
DHLTNK12-17	0.06396	0.00219	1.11322	0.03848	0.12451	0.00207	739	73	760	18	756	12	324	476	0.68	99
DHLTNK12-18	0.06877	0.00301	1.44766	0.06228	0.14973	0.00217	900	95	909	26	899	12	206	170	1.21	98
DHLTNK12-19	0.06468	0.00358	1.10975	0.03915	0.12699	0.00227	765	117	758	19	771	13	215	254	0.85	98
DHLTNK12-20	0.07117	0.00286	1.60085	0.06461	0.16195	0.00284	962	81	971	25	968	16	61	94	0.65	99
DHLTNK12-21	0.07074	0.00419	1.47915	0.05928	0.15435	0.00271	950	117	922	24	925	15	94	150	0.62	99
DHLTNK12-22	0.06692	0.00304	1.25562	0.05142	0.13667	0.00238	835	94	826	23	826	14	73	120	0.61	99
DHLTNK12-23	0.06658	0.00347	1.25421	0.06089	0.13660	0.00206	833	105	825	27	825	12	107	85	1.26	99

Table 2 (*continued*)

Spots	Isotopic ratios						Apparent age (Ma)						Th	U	Th/U	Con.
	$^{207}Pb/^{206}Pb$	1σ	$^{207}Pb/^{235}U$	1σ	$^{206}Pb/^{238}U$	1σ	$^{207}Pb/^{206}Pb$	1σ	$^{207}Pb/^{235}U$	1σ	$^{206}Pb/^{238}U$	1σ	(ppm)			
DHLTNK12-24	0.07567	0.00236	1.91598	0.05944	0.18354	0.00305	1087	57	1087	21	1086	17	147	180	0.81	99
DHLTNK12-25	0.06212	0.00403	0.91097	0.06225	0.10781	0.00216	680	106	658	33	660	13	56	60	0.94	99
DHLTNK12-26	0.06446	0.00181	1.17996	0.03753	0.13126	0.00167	767	60	791	17	795	10	289	394	0.73	99
DHLTNK12-27	0.07049	0.00248	1.50339	0.05271	0.15479	0.00191	943	68	932	21	928	11	214	253	0.85	99
DHLTNK12-28	0.06104	0.00193	0.86479	0.02707	0.10177	0.00108	640	67	633	15	625	6	456	383	1.19	98
DHLTNK12-29	0.06208	0.00224	0.94525	0.03268	0.11060	0.00164	676	78	676	17	676	10	84	139	0.60	99
DHLTNK12-30	0.12170	0.00259	6.07857	0.13655	0.35975	0.00432	1981	39	1987	20	1981	20	217	250	0.87	99
DHLTNK12-31	0.08634	0.00569	1.14928	0.06625	0.09927	0.00197	1346	160	777	31	610	12	30	51	0.58	75
DHLTNK12-32	0.07058	0.00219	1.55002	0.04948	0.15853	0.00195	946	65	950	20	949	11	100	132	0.76	99
DHLTNK12-33	0.06750	0.00207	1.30353	0.04038	0.14028	0.00203	854	65	847	18	846	11	86	147	0.59	99
DHLTNK12-34	0.07522	0.00223	1.86342	0.05155	0.17990	0.00274	1076	60	1068	18	1066	15	183	170	1.08	99
DHLTNK12-35	0.06135	0.00218	0.93596	0.03318	0.10990	0.00139	650	78	671	17	672	8	126	133	0.94	99
DHLTNK12-36	0.06481	0.00257	1.14623	0.04387	0.12775	0.00169	769	83	775	21	775	10	77	114	0.67	99
DHLTNK12-37	0.11132	0.00417	4.95265	0.14702	0.32403	0.00507	1821	68	1811	25	1809	25	104	109	0.96	99
DHLTNK12-38	0.06647	0.00181	1.27237	0.03119	0.13803	0.00170	820	56	833	14	833	10	426	1332	0.32	99
DHLTNK12-39	0.07104	0.00220	1.60227	0.05024	0.16234	0.00191	958	63	971	20	970	11	100	159	0.63	99
DHLTNK12-40	0.11085	0.00303	5.00362	0.14225	0.32424	0.00343	1813	50	1820	24	1810	17	98	84	1.17	99
DHLTNK12-41	0.06701	0.00194	1.31306	0.03975	0.14099	0.00164	839	61	851	17	850	9	296	260	1.14	99
DHLTNK12-42	0.06128	0.00206	0.90332	0.03023	0.10682	0.00125	650	72	654	16	654	7	154	175	0.88	99
DHLTNK12-43	0.06843	0.00293	1.28005	0.05386	0.13582	0.00165	883	89	837	24	821	9	75	65	1.14	98
DHLTNK12-44	0.06274	0.00174	0.99156	0.02823	0.11403	0.00121	698	64	700	14	696	7	200	456	0.44	99
DHLTNK12-45	0.06675	0.00207	1.27842	0.04233	0.13797	0.00192	831	65	836	19	833	11	199	260	0.76	99
DHLTNK12-46	0.05943	0.00171	0.79286	0.02309	0.09632	0.00115	583	61	593	13	593	7	503	514	0.98	99
DHLTNK12-47	0.06146	0.00204	0.90560	0.03035	0.10645	0.00127	655	70	655	16	652	7	171	220	0.78	99
DHLTNK12-48	0.06261	0.00381	0.94030	0.05687	0.10963	0.00172	694	130	673	30	671	10	48	52	0.91	99
DHLTNK12-49	0.06750	0.00242	1.30612	0.04843	0.13931	0.00181	854	76	848	21	841	10	45	91	0.49	99
DHLTNK12-50	0.10828	0.00356	4.75583	0.15530	0.31723	0.00409	1772	60	1777	27	1776	20	78	87	0.90	99
DHLTNK12-51	0.06766	0.00284	1.32738	0.05425	0.14220	0.00190	857	87	858	24	857	11	37	68	0.55	99
DHLTNK12-52	0.07261	0.00194	1.57670	0.04223	0.15629	0.00149	1003	55	961	17	936	8	473	652	0.73	97
DHLTNK12-53	0.06671	0.00258	1.24756	0.04673	0.13620	0.00201	828	80	822	21	823	11	84	87	0.96	99
DHLTNK12-54	0.07239	0.00257	1.06989	0.04232	0.10589	0.00133	998	105	739	21	649	8	285	370	0.77	87
DHLTNK12-55	0.06011	0.00333	0.82013	0.04483	0.09941	0.00144	609	120	608	25	611	8	79	66	1.18	99
DHLTNK12-56	0.07465	0.00222	1.64724	0.04970	0.15864	0.00151	1059	60	988	19	949	8	312	292	1.07	95
DHLTNK12-57	0.07215	0.00199	1.63247	0.04478	0.16298	0.00146	991	61	983	17	973	8	402	409	0.98	99
DHLTNK12-58	0.07551	0.00188	1.84157	0.04592	0.17559	0.00156	1083	50	1060	16	1043	9	291	601	0.48	98
DHLTNK12-59	0.15971	0.00421	10.27546	0.27464	0.46322	0.00456	2454	46	2460	25	2454	20	87	98	0.89	99
DHLTNK12-60	0.06934	0.00221	0.82653	0.02495	0.08653	0.00104	909	65	612	14	535	6	181	298	0.61	86
DHLTNK12-61	0.06720	0.00233	1.28807	0.04133	0.13948	0.00197	844	72	840	18	842	11	125	312	0.40	99
DHLTNK12-62	0.07310	0.00203	1.75485	0.04900	0.17245	0.00176	1017	56	1029	18	1026	10	302	404	0.75	99
DHLTNK12-63	0.07092	0.00345	1.52339	0.06718	0.15628	0.00223	955	99	940	27	936	12	36	105	0.34	99
DHLTNK12-64	0.06221	0.00271	0.96402	0.04215	0.11118	0.00130	681	93	685	22	680	8	86	191	0.45	99
DHLTNK12-65	0.06108	0.00239	0.90505	0.03587	0.10646	0.00131	643	79	654	19	652	8	94	205	0.46	99
DHLTNK12-66	0.15992	0.00589	10.13233	0.38083	0.45888	0.00777	2455	62	2447	35	2435	34	17	16	1.09	99
DHLTNK12-67	0.06570	0.00259	1.20206	0.04755	0.13203	0.00174	798	78	802	22	799	10	126	101	1.26	99
DHLTNK12-68	0.16769	0.00426	11.34922	0.30680	0.48610	0.00602	2535	43	2552	25	2554	26	64	265	0.24	99
DHLTNK12-69	0.06426	0.00261	1.09876	0.04379	0.12363	0.00139	750	87	753	21	751	8	98	127	0.77	99
DHLTNK12-70	0.06516	0.00328	1.14575	0.05381	0.12870	0.00166	789	75	775	25	780	9	59	95	0.62	99
DHLTNK12-71	0.06425	0.00225	1.10905	0.04091	0.12404	0.00154	750	79	758	20	754	9	122	169	0.72	99
DHLTNK12-72	0.06108	0.00204	0.91993	0.03035	0.10840	0.00103	643	77	662	16	663	6	84	275	0.31	99
DHLTNK12-73	0.06642	0.00229	1.02524	0.03664	0.11098	0.00141	820	77	717	18	678	8	123	250	0.49	94
DHLTNK12-74	0.07194	0.00298	1.64182	0.06856	0.16563	0.00284	983	84	986	26	988	16	71	57	1.23	99
DHLTNK12-75	0.11404	0.00306	5.33721	0.14369	0.33541	0.00353	1865	53	1875	23	1865	17	107	117	0.91	99
DHLTNK12-76	0.06617	0.00271	1.20831	0.04946	0.13182	0.00187	813	85	804	23	798	11	66	88	0.75	99

(*continued on next page*)

Table 2 (*continued*)

Spots	Isotopic ratios						Apparent age (Ma)						Th	U	Th/U	Con.
	$^{207}Pb/^{206}Pb$	1σ	$^{207}Pb/^{235}U$	1σ	$^{206}Pb/^{238}U$	1σ	$^{207}Pb/^{206}Pb$	1σ	$^{207}Pb/^{235}U$	1σ	$^{206}Pb/^{238}U$	1σ	(ppm)			
DHLTNK12-77	0.07756	0.00285	2.09611	0.07712	0.19523	0.00272	1144	73	1148	25	1150	15	72	74	0.97	99
DHLTNK12-78	0.16001	0.00414	8.37569	0.21747	0.37509	0.00319	2457	43	2273	24	2053	15	600	1151	0.52	89
DHLTNK12-79	0.07768	0.00253	1.86890	0.06099	0.17295	0.00192	1139	97	1070	22	1028	11	313	330	0.95	96
DHLTNK12-80	0.07758	0.00253	2.07187	0.06884	0.19166	0.00207	1136	65	1140	23	1130	11	262	460	0.57	99
DHLTNK12-81	0.07596	0.00336	1.74296	0.07129	0.16878	0.00264	1094	89	1025	26	1005	15	35	71	0.49	98
DHLTNK12-82	0.24028	0.00602	20.48349	0.51050	0.61249	0.00567	3122	40	3114	24	3080	23	68	93	0.73	98
DHLTNK12-83	0.06974	0.00305	1.46023	0.06404	0.15130	0.00212	920	91	914	26	908	12	34	53	0.64	99
DHLTNK12-84	0.06063	0.00149	0.83879	0.02165	0.09906	0.00106	628	54	618	12	609	6	327	900	0.36	98
DHLTNK12-85	0.06218	0.00255	0.96813	0.03878	0.11249	0.00136	680	87	687	20	687	8	55	95	0.57	99
DHLTNK12-86	0.06014	0.00183	0.83527	0.02645	0.10011	0.00142	609	65	617	15	615	8	244	278	0.88	99
DHLTNK12-87	0.07182	0.00246	1.61054	0.05291	0.16244	0.00180	981	70	974	21	970	10	99	144	0.69	99
DHLTNK12-88	0.07060	0.00386	1.31064	0.07113	0.13607	0.00204	946	112	850	31	822	12	20	48	0.42	96
DHLTNK12-89	0.06492	0.00186	1.06947	0.03081	0.11863	0.00109	772	61	738	15	723	6	314	1014	0.31	97
DHLTNK12-90	0.16593	0.00398	10.36821	0.26416	0.44953	0.00487	2517	40	2468	24	2393	22	167	592	0.28	96
DHLTNK12-91	0.06130	0.00248	0.87596	0.03433	0.10377	0.00118	650	92	639	19	636	7	77	141	0.54	99
DHLTNK12-92	0.12842	0.00335	6.77610	0.16932	0.38269	0.00494	2076	45	2083	22	2089	23	109	221	0.49	99
DHLTNK12-93	0.06326	0.00309	0.92925	0.04512	0.10734	0.00164	717	104	667	24	657	10	50	96	0.52	98
DHLTNK12-94	0.06996	0.00292	1.46165	0.04753	0.15348	0.00225	928	86	915	20	920	13	163	216	0.75	99
DHLTNK12-95	0.06561	0.00209	1.19420	0.03594	0.13250	0.00161	794	67	798	17	802	9	128	216	0.59	99
DHLTNK12-96	0.15305	0.00346	9.57888	0.24008	0.45088	0.00575	2381	38	2395	23	2399	26	170	476	0.36	99
DHLTNK12-97	0.06094	0.00218	0.87806	0.03142	0.10446	0.00116	639	78	640	17	641	7	107	186	0.58	99
DHLTNK12-98	0.07212	0.00192	1.66048	0.04563	0.16677	0.00230	991	21	994	17	994	13	319	945	0.34	99

Table 3
REE analysis of the zircons.

REE spots	La ppm	Ce ppm	Pr ppm	Nd ppm	Sm ppm	Eu ppm	Gd ppm	Tb ppm	Dy ppm	Ho ppm	Er ppm	Tm ppm	Yb ppm	Lu ppm
Sample DHLTNP-7: Gray medium-grained porphyritic biotite-quartz monzonite														
DHLTNP0-7-5	1.62	20.28	0.62	4.06	4.84	0.01	37.36	16.51	227.15	94.77	441.59	94.16	858.42	166.22
DHLTNP-7-6	3.01	23.37	1.50	9.89	7.75	0.03	33.93	13.82	189.13	78.92	367.10	79.71	740.26	147.34
DHLTNP-7-8	0.85	17.21	0.39	2.21	4.93	0.06	39.60	17.00	236.85	98.29	457.27	98.74	903.39	179.28
DHLTNP-7-10	0.44	14.00	0.13	1.38	4.13	0.05	30.19	12.25	166.03	69.20	324.60	71.68	653.33	129.70
DHLTNP-7-12	1.46	17.86	0.60	3.67	4.68	0.03	34.06	14.35	197.06	80.53	382.56	82.38	754.06	149.00
DHLTNP-7-13	12.98	50.80	4.35	22.49	10.58	0.10	44.83	18.03	243.70	99.03	459.52	97.55	881.55	172.13
DHLTNP-7-15	1.29	20.45	1.04	6.74	6.06	0.19	35.57	14.21	188.00	75.32	349.79	74.91	684.51	135.97
DHLTNP-7-16	2.37	20.15	1.67	12.10	9.43	0.51	35.71	12.21	141.01	52.67	243.09	52.48	484.29	99.31
DHLTNP-7-17	0.03	12.97	0.06	1.14	3.16	0.11	25.74	10.32	142.43	58.67	277.27	59.61	549.08	110.68
DHLTNP-7-22	9.58	37.15	3.58	18.54	8.09	0.06	31.03	11.69	161.21	65.72	319.91	68.99	665.61	122.81
DHLTNP-7-24	7.14	28.60	2.51	12.26	6.49	0.05	32.58	13.22	187.97	77.97	384.88	83.58	789.79	148.79
DHLTNP-7-25	13.42	45.93	4.23	21.00	7.91	0.11	33.07	12.35	166.09	66.28	320.02	67.74	642.98	119.31
DHLTNP-7-27	1.60	22.14	1.91	13.85	8.18	0.12	34.20	12.92	172.80	69.23	338.73	72.71	706.31	132.77
DHLTNP-7-28	1.68	18.20	0.79	3.83	4.48	0.08	31.55	12.82	177.80	72.45	349.28	74.51	704.42	131.01
DHLTNP-7-29	1.17	22.32	0.49	3.75	6.67	0.07	51.30	21.54	296.38	119.07	563.89	117.71	1104.26	201.57
DHLTNP-7-30	2.18	15.92	0.89	5.75	3.95	0.06	22.21	8.54	118.45	48.63	234.11	50.38	482.61	89.66
Sample DHLTNP: Pink-gray medium-fine grained biotite-quartz monzonite														
DHLTNP-1	2.64	20.55	1.01	6.86	4.39	0.11	26.01	10.20	136.82	57.11	267.85	59.96	561.35	100.34
DHLTNP-2	0.37	15.16	0.22	2.31	5.04	0.05	40.40	18.09	250.26	104.17	492.06	109.15	1031.79	187.14
DHLTNP-3	1.55	16.27	0.34	2.87	3.67	0.15	23.39	9.53	129.29	52.86	252.17	55.80	531.52	95.99
DHLTNP-4	2.67	31.00	1.25	7.23	7.76	0.23	48.19	19.81	256.36	104.85	477.72	103.51	956.09	171.81
DHLTNP-6	10.48	40.13	4.39	23.16	8.89	0.05	29.85	10.37	135.96	55.62	258.84	58.20	553.52	101.76
DHLTNP-9	4.84	26.49	2.61	16.26	10.76	0.25	36.77	12.00	140.42	53.94	237.49	52.73	494.58	89.23
DHLTNP-10	14.95	48.02	4.13	19.36	7.21	0.08	36.94	15.97	217.66	89.37	420.68	93.41	868.34	161.17
DHLTNP-12	6.65	37.38	2.91	16.28	8.84	0.08	44.07	17.78	241.03	98.87	466.92	103.52	973.65	175.78
DHLTNP-13	5.80	35.38	2.49	15.06	8.41	0.08	41.63	17.15	232.44	94.71	442.35	99.28	917.22	167.02
DHLTNP-14	1.64	21.15	0.81	5.72	7.40	0.07	44.29	17.11	233.97	95.72	448.12	98.79	917.80	164.68
DHLTNP-16	7.59	40.05	4.56	24.61	10.17	0.10	36.45	13.63	176.65	72.44	342.99	76.84	716.24	132.85
DHLTNP-18	11.00	48.57	4.56	24.57	12.12	0.08	49.31	18.73	247.31	102.26	473.52	103.96	979.99	172.96
DHLTNP-19	1.22	15.87	0.71	3.63	4.09	0.04	27.71	11.55	160.49	67.60	321.42	72.79	690.07	124.03
DHLTNP-21	57.22	144.39	17.27	76.93	23.98	0.17	52.70	16.63	196.78	78.60	358.66	78.28	735.94	133.35
Sample SC: Metagabbro														
SC-2	18.72	66.52	7.15	38.73	14.78	0.09	50.26	18.13	233.40	94.81	440.51	96.53	895.85	163.82
SC-4	78.44	230.93	31.27	169.43	48.95	0.44	77.35	19.35	199.18	71.37	313.65	67.47	626.63	112.00
SC-5	10.77	43.15	5.22	31.09	16.05	0.62	45.07	12.97	147.26	56.25	249.69	54.14	503.89	94.24
SC-7	6.61	28.49	2.70	14.83	8.86	0.13	42.07	18.13	245.80	102.46	495.77	111.06	1046.97	191.23
SC-9	3.85	25.35	1.80	9.15	4.23	0.13	26.98	9.74	127.45	53.82	244.78	54.77	515.07	96.04
SC-11	1.81	18.84	1.01	5.23	4.43	0.03	26.91	11.23	146.94	61.22	297.49	65.62	622.39	114.03
SC-12	2.17	25.68	1.38	8.02	7.56	0.19	39.27	14.08	176.27	69.96	322.61	67.90	629.90	117.20
SC-14	1.16	15.77	0.51	3.03	4.15	0.06	27.85	11.77	161.68	67.09	315.08	70.55	662.60	120.60
SC-15	14.70	62.16	6.85	35.12	15.36	0.08	57.27	20.51	268.03	107.60	496.26	107.54	988.83	178.54
SC-16	0.03	13.45	0.08	0.89	3.59	0.03	28.10	12.71	175.53	73.73	348.00	76.01	714.85	126.81
SC-17	12.32	43.57	4.46	23.01	9.72	0.04	36.50	14.05	182.28	73.96	341.47	74.49	692.34	124.25
SC-18	6.83	43.55	5.31	31.50	13.64	0.11	40.96	13.75	180.13	70.36	337.96	72.10	678.30	125.35
SC-19	3.49	37.69	1.79	12.85	15.21	0.80	91.53	42.35	560.61	200.80	911.42	188.26	1695.83	283.57
SC-21	3.37	22.73	1.33	7.97	5.41	0.08	30.44	12.46	167.76	68.42	333.76	71.38	680.65	125.85
SC-22	0.13	11.81	0.08	1.54	3.17	0.07	22.94	9.59	133.08	55.16	266.60	58.94	604.40	110.68
SC-23	16.18	40.57	3.25	14.69	5.30	0.09	22.15	8.71	115.42	47.21	226.51	49.41	474.71	89.69
SC-24	46.73	128.91	15.54	80.74	25.85	0.13	64.56	21.29	271.87	106.25	504.13	106.25	1003.19	182.50
SC-25	0.81	13.54	0.38	2.66	4.14	0.07	33.08	14.38	206.71	84.77	418.75	91.44	891.50	163.71
Sample DHLT92: Silicified calcitic marble														
DHLT92-1	0.02	64.65	0.09	1.78	3.83	0.77	25.18	9.18	105.02	39.90	172.15	34.71	312.19	61.49
DHLT92-2	0.12	16.84	0.33	4.14	7.39	2.05	48.91	15.79	186.60	70.68	313.32	63.23	563.37	113.46
DHLT92-4	4.60	30.89	1.14	5.31	3.98	0.86	18.70	6.66	81.78	33.41	167.22	39.14	397.47	86.32
DHLT92-5	2.79	62.52	1.38	8.75	10.28	2.32	52.71	18.29	227.56	91.54	433.54	93.93	903.15	186.84
DHLT92-6	5.62	55.32	3.73	27.08	16.14	2.26	55.12	16.79	187.03	70.15	310.77	66.73	628.66	126.18
DHLT92-8	0.16	4.22	0.19	5.22	8.78	0.32	52.84	17.82	206.95	73.49	298.14	58.25	492.09	93.21
DHLT92-9	0.23	54.06	0.57	8.01	9.56	3.10	34.20	8.60	84.41	27.16	110.82	21.29	196.58	38.49
DHLT92-10	28.13	82.04	9.70	49.48	12.65	1.04	23.29	6.29	64.27	23.89	105.13	22.03	203.09	41.08
DHLT92-11	0.06	3.15	0.01	1.02	1.84	0.10	13.49	6.27	89.48	36.96	194.30	45.86	464.39	95.39
DHLT92-13	0.01	10.44	0.03	1.40	1.68	0.29	12.75	4.32	54.36	20.53	95.20	20.59	197.53	41.08
DHLT92-14	0.26	16.55	0.43	9.15	16.86	0.39	70.90	20.87	231.44	80.78	332.18	62.88	528.54	94.67
DHLT92-15	2.51	14.43	1.24	9.73	10.21	2.09	31.66	7.22	50.00	10.55	29.23	4.77	36.54	5.82
DHLT92-17	0.01	9.52	0.02	0.90	1.12	0.53	6.62	2.29	29.22	13.36	70.81	18.45	211.95	52.62
DHLT92-23	0.02	11.97	0.12	1.85	5.08	0.61	29.21	9.66	119.38	45.60	198.82	38.23	349.33	66.59
DHLT92-24	0.04	12.63	0.10	1.66	2.15	0.71	15.72	5.98	77.30	30.19	141.25	29.88	286.64	59.00
DHLT92-25	2.66	35.73	1.17	10.64	15.33	0.73	76.22	23.62	274.70	98.60	408.75	76.53	666.33	125.48
DHLT92-26	0.11	16.50	0.37	3.86	8.11	0.87	39.16	11.32	122.56	41.76	169.36	32.37	290.18	55.52
DHLT92-28	0.33	8.44	0.12	1.49	3.15	0.35	18.22	6.01	69.27	24.96	110.31	22.94	204.76	38.11
DHLT92-29	0.03	11.56	0.18	2.74	5.58	0.24	29.97	10.17	117.80	42.46	177.26	35.55	313.48	56.27

(*continued on next page*)

Table 3 (*continued*)

REE spots	La ppm	Ce ppm	Pr ppm	Nd ppm	Sm ppm	Eu ppm	Gd ppm	Tb ppm	Dy ppm	Ho ppm	Er ppm	Tm ppm	Yb ppm	Lu ppm
DHLT92-30	9.18	47.12	3.08	18.82	10.48	2.76	25.54	5.97	51.52	15.12	57.22	11.24	100.99	18.26
DHLT92-31	1.26	16.98	0.40	3.11	2.58	0.17	16.73	6.05	76.91	30.66	139.60	30.15	284.23	52.27
DHLT92-32	0.26	16.16	0.05	1.09	1.96	0.35	8.71	2.75	33.29	12.85	57.88	13.02	126.45	25.75
DHLT92-33	0.02	6.09	0.12	2.47	5.47	1.10	34.16	12.07	155.08	62.06	277.87	57.24	517.12	98.96
DHLT92-34	1.71	88.93	1.43	15.10	19.04	4.34	74.35	20.69	211.76	69.11	275.68	53.13	457.26	86.40
DHLT92-35	0.50	22.91	0.15	1.25	1.78	0.75	9.35	3.47	46.45	19.95	103.47	26.53	283.26	61.89
DHLT92-36	3.49	21.77	1.14	8.36	7.52	0.75	40.43	14.05	169.83	65.68	292.08	59.68	534.62	103.60
DHLT92-37	2.88	22.16	1.20	7.49	6.63	0.69	32.88	10.46	122.35	45.02	194.94	39.14	350.64	62.73
DHLT92-38	0.18	10.20	0.13	2.18	3.82	0.17	18.03	5.63	63.32	22.78	98.83	19.93	182.33	32.21
DHLT92-40	0.02	4.56	0.09	1.74	2.17	1.08	8.75	2.36	26.47	9.60	45.00	10.52	105.97	23.79
DHLT92-41	0.02	14.55	0.15	3.64	8.30	2.19	50.14	17.89	225.80	88.72	405.13	83.39	765.46	147.73
DHLT92-42	0.01	10.46	0.06	0.64	1.69	0.31	9.65	3.65	43.51	16.73	77.65	16.20	150.06	28.27
DHLT92-43	0.02	1.86	0.08	1.04	3.23	0.17	19.58	6.78	82.09	31.72	143.84	29.76	279.50	53.93
DHLT92-44	0.12	21.34	0.07	1.47	3.58	0.88	25.42	10.19	137.08	56.32	275.06	63.85	641.67	136.75
DHLT92-47	31.09	85.86	8.96	40.49	10.05	1.05	21.62	5.78	64.21	24.20	104.24	22.80	210.85	42.41
DHLT92-48	0.02	11.72	0.06	0.94	2.50	0.29	14.31	5.08	61.59	22.88	103.26	21.92	194.22	35.13
DHLT92-59	0.86	32.82	0.43	4.31	5.44	1.55	27.89	10.22	129.12	52.81	255.35	56.30	551.65	108.43
DHLT92-53	0.03	25.92	0.06	1.10	1.75	0.66	6.21	2.02	22.23	8.24	38.70	8.51	89.89	17.84
DHLT92-55	0.73	15.30	0.35	3.52	5.73	0.86	36.28	13.19	163.99	62.82	277.29	57.29	522.77	99.25
DHLT92-57	922.57	2205.77	285.89	1335.79	278.47	6.27	336.49	67.95	570.81	169.40	606.12	106.10	826.72	130.15
DHLT92-58	0.05	32.06	0.11	1.92	4.30	0.59	27.22	10.91	134.14	54.41	259.98	56.97	549.53	110.49
DHLT92-59	0.01	30.89	0.10	1.64	2.39	0.32	11.26	3.61	42.45	16.36	73.88	16.88	161.57	31.79
DHLT92-60	0.05	4.86	0.15	3.23	7.79	0.89	44.32	15.04	181.50	68.65	296.54	59.97	533.44	101.48
DHLT92-61	0.57	7.33	0.22	1.76	2.13	0.37	12.82	4.39	51.84	19.06	79.51	15.85	139.51	25.95
DHLT92-62	1.72	11.44	0.48	3.51	4.25	0.28	20.53	6.69	76.23	28.24	119.40	23.83	208.26	37.79
DHLT92-64	0.51	3.94	0.51	5.84	9.08	1.02	43.05	14.36	169.46	62.92	261.47	50.86	450.30	84.99
DHLT92-65	0.05	1.96	0.05	1.01	3.01	0.12	23.27	9.53	119.49	46.42	210.54	44.73	406.74	76.43
DHLT92-66	0.11	15.76	0.14	2.80	5.64	0.48	31.44	10.54	126.51	48.63	216.94	43.69	400.80	77.00
DHLT92-67	0.40	16.80	0.31	3.63	5.53	0.55	30.21	10.43	122.65	45.83	198.53	40.33	349.96	61.09
DHLT92-68	0.25	12.91	0.40	6.15	10.58	0.80	53.27	17.22	197.47	71.43	304.26	61.23	544.83	98.06
DHLT92-69	3.31	10.21	1.25	10.36	12.97	1.15	55.52	15.61	161.94	55.50	219.25	40.49	347.77	65.03
DHLT92-71	0.07	3.18	0.14	2.59	5.69	0.54	30.39	11.12	127.34	48.45	217.92	44.62	403.46	79.52
DHLT92-72	0.20	9.90	0.08	1.72	4.44	0.11	30.32	12.58	164.54	65.32	301.13	64.54	593.59	107.43
DHLT92-73	28.02	74.14	7.96	38.19	11.37	1.40	27.05	7.74	86.76	30.76	130.64	25.82	228.93	43.89
DHLT92-75	4.26	21.30	1.35	7.74	5.58	0.49	24.27	7.62	89.27	32.28	142.96	28.92	257.55	48.60
DHLT92-76	0.07	102.24	0.41	5.66	7.73	3.70	26.27	6.55	59.67	17.87	66.55	12.69	113.37	20.65
DHLT92-77	0.03	7.42	0.30	4.71	7.54	0.48	29.56	8.79	94.43	31.78	130.85	25.27	226.92	41.19
DHLT92-78	8.29	37.18	1.94	10.40	3.89	0.78	16.37	5.71	73.15	30.84	158.33	38.02	397.78	86.71
DHLT92-79	0.11	33.77	0.15	2.17	3.91	1.30	22.50	7.57	93.93	35.69	160.18	33.15	305.29	60.18
DHLT92-80	4.95	18.13	2.19	15.82	12.77	1.82	59.94	19.92	243.77	92.23	407.91	80.96	729.87	140.38
DHLT92-81	4.59	16.79	1.56	11.89	11.08	0.86	45.62	13.53	146.73	50.66	200.99	38.71	338.38	61.68
Sample DHLTNK12: Chloritoid–muscovite schist														
DHLTNK12-1	0.14	116.16	0.78	10.61	21.07	5.75	118.10	40.07	469.16	170.48	731.50	149.53	1327.91	255.89
DHLTNK12-2	0.09	37.79	0.26	4.96	8.55	3.59	34.58	10.01	102.42	34.28	142.45	29.49	276.90	54.96
DHLTNK12-3	0.71	34.34	0.99	10.67	13.87	2.63	72.11	23.15	264.84	97.45	414.99	83.79	732.60	140.80
DHLTNK12-5	0.08	5.15	0.21	4.12	7.77	3.39	50.33	15.54	174.07	60.83	245.88	47.46	404.68	77.17
DHLTNK12-6	0.01	17.85	0.04	0.82	1.55	0.30	10.45	3.65	48.92	19.50	92.26	20.67	197.70	40.54
DHLTNK12-7	0.34	13.48	0.19	2.15	4.53	0.54	22.24	7.02	79.91	29.03	123.60	24.61	216.25	42.76
DHLTNK12-10	0.02	37.91	0.09	1.20	2.85	1.49	19.78	6.04	72.79	28.58	135.90	29.52	291.63	62.00
DHLTNK12-11	0.08	16.56	0.16	2.55	4.94	0.37	26.60	8.73	99.15	36.56	157.86	31.37	279.75	54.07
DHLTNK12-12	2.41	30.88	0.69	5.07	2.38	1.24	13.98	4.73	55.28	22.24	110.11	25.91	270.37	61.15
DHLTNK12-14	0.02	15.34	0.04	0.69	1.12	0.99	6.02	2.81	37.68	16.79	91.75	23.62	276.03	71.55
DHLTNK12-15	0.02	2.96	0.16	4.30	7.76	0.41	47.54	16.49	195.91	72.09	311.79	63.95	569.96	110.07
DHLTNK12-16	0.11	3.36	0.26	4.15	9.02	0.47	49.00	16.37	195.55	70.77	307.93	62.73	552.45	106.02
DHLTNK12-17	0.03	24.98	0.05	0.75	2.01	1.02	11.30	4.06	48.20	19.94	104.16	24.75	274.96	65.15
DHLTNK12-18	50.06	133.39	16.49	74.19	17.90	4.02	36.31	8.47	88.22	30.31	131.39	27.20	257.87	53.04
DHLTNK12-20	0.18	10.29	0.11	1.03	2.72	0.36	17.56	7.25	87.97	34.62	158.13	33.47	307.50	60.45
DHLTNK12-21	1.04	13.63	0.35	2.64	4.00	1.04	27.58	9.87	120.83	47.18	212.33	43.97	402.86	81.20
DHLTNK12-22	0.01	24.59	0.06	1.07	2.93	0.99	22.93	8.32	113.59	46.35	226.59	50.58	496.19	105.32
DHLTNK12-23	0.03	21.89	0.35	4.94	10.10	2.80	48.82	14.88	161.71	57.47	248.32	47.51	420.95	83.50
DHLTNK12-25	0.02	50.39	0.11	2.26	5.00	1.67	23.67	7.52	85.30	31.43	139.33	29.23	275.13	53.62
DHLTNK12-26	1.42	42.35	0.42	2.46	2.03	1.38	14.01	4.74	54.84	22.58	112.26	26.29	283.17	69.59
DHLTNK12-28	3.02	56.34	1.10	8.86	8.77	2.10	37.03	11.70	129.36	47.85	208.79	44.22	406.94	78.15
DHLTNK12-29	0.03	14.58	0.16	3.11	4.49	0.73	15.65	4.13	40.50	13.17	53.61	10.78	97.68	18.33
DHLTNK12-30	0.02	31.32	0.16	3.17	6.41	0.96	29.37	8.79	95.53	33.00	135.43	27.53	244.52	45.15
DHLTNK12-32	0.02	18.14	0.10	1.73	3.25	1.20	13.47	4.30	48.48	18.58	88.83	20.28	207.86	45.69
DHLTNK12-33	0.04	6.77	0.04	1.25	3.44	0.96	23.02	8.23	102.52	40.86	189.49	40.75	398.30	80.12
DHLTNK12-34	0.02	10.65	0.32	5.51	10.10	0.78	43.92	12.98	138.70	46.47	188.78	36.27	307.34	54.05
DHLTNK12-35	0.09	6.52	0.35	5.74	14.41	5.80	93.91	29.12	317.20	106.72	431.93	82.17	705.09	125.99
DHLTNK12-36	0.11	5.98	0.11	1.98	4.12	0.59	24.80	8.79	109.21	41.05	184.07	37.47	338.12	63.63
DHLTNK12-37	0.04	2.50	0.23	3.94	6.92	0.08	35.35	10.53	112.09	37.59	151.30	28.90	239.51	42.06
DHLTNK12-39	3.22	17.90	1.22	7.97	6.28	0.22	29.28	10.03	121.59	45.37	199.10	41.33	371.01	68.16
DHLTNK12-40	4.92	21.58	1.90	12.01	8.43	0.96	34.48	10.12	109.51	38.56	159.14	31.48	272.53	50.64

Table 3 (*continued*)

REE spots	La ppm	Ce ppm	Pr ppm	Nd ppm	Sm ppm	Eu ppm	Gd ppm	Tb ppm	Dy ppm	Ho ppm	Er ppm	Tm ppm	Yb ppm	Lu ppm
DHLTNK12-41	0.14	43.10	0.83	11.46	14.03	2.83	54.13	16.75	195.48	73.91	330.64	68.97	629.77	124.01
DHLTNK12-42	6.27	35.49	2.46	16.46	12.99	0.36	67.23	21.83	248.85	90.20	363.92	67.74	554.81	98.35
DHLTNK12-44	2.40	19.91	0.65	2.57	2.68	0.26	16.18	6.77	92.39	39.36	201.40	46.11	455.59	88.76
DHLTNK12-45	0.82	47.91	0.85	8.99	11.74	5.35	71.09	24.56	303.53	118.15	535.84	113.22	1081.61	207.84
DHLTNK12-46	0.11	57.24	0.18	2.97	5.63	2.14	28.13	9.40	102.28	36.66	162.35	36.89	368.19	73.55
DHLTNK12-47	56.63	141.85	13.96	61.97	12.15	1.89	21.05	5.23	55.75	21.10	99.24	22.52	229.35	45.92
DHLTNK12-48	0.07	9.88	0.07	1.26	2.15	1.21	10.61	3.31	35.08	12.69	59.39	13.55	143.72	31.62
DHLTNK12-49	0.01	6.49	0.16	2.11	3.41	1.28	16.78	5.17	60.62	22.82	107.08	24.32	248.22	53.31
DHLTNK12-50	0.01	7.55	0.11	2.17	3.54	0.60	18.80	6.28	76.95	29.82	131.60	27.60	251.90	48.36
DHLTNK12-53	0.03	23.39	0.18	4.21	9.10	5.90	54.71	16.97	201.62	79.75	343.61	71.35	663.14	132.39
DHLTNK12-55	0.16	24.59	0.59	9.63	11.37	5.06	33.88	8.08	72.46	22.77	87.37	17.35	153.77	28.35
DHLTNK12-57	0.11	39.86	1.11	17.52	31.89	0.84	131.59	34.37	335.61	108.17	420.26	79.28	691.60	135.84
DHLTNK12-58	0.01	14.82	0.04	1.06	2.76	1.02	18.70	6.52	79.39	32.10	157.12	36.09	371.77	81.69
DHLTNK12-59	1.70	13.03	0.65	5.89	7.87	1.26	34.67	10.73	119.98	42.02	174.66	34.40	299.05	55.09
DHLTNK12-61	3.09	17.88	1.00	5.83	3.81	0.59	19.38	6.95	92.23	38.39	186.65	43.52	436.19	88.83
DHLTNK12-62	0.03	3.65	0.17	3.15	7.63	0.15	49.26	18.14	215.13	77.82	327.49	63.83	542.64	94.47
DHLTNK12-63	0.04	4.72	0.03	0.58	2.05	0.19	15.56	6.38	85.60	35.54	172.69	39.30	384.71	75.59
DHLTNK12-64	0.16	18.65	0.18	1.76	3.77	0.84	19.84	6.50	78.11	30.22	143.09	30.89	301.24	60.86
DHLTNK12-65	4.11	27.62	1.06	5.62	5.35	1.24	24.35	7.86	91.05	34.68	162.33	35.04	338.01	67.66
DHLTNK12-67	0.26	28.15	0.18	2.81	4.77	1.01	22.15	7.25	87.35	32.58	152.10	33.71	331.63	66.37
DHLTNK12-68	1.25	37.71	0.23	2.45	3.05	0.72	14.58	4.71	56.12	22.00	103.90	24.18	247.05	49.50
DHLTNK12-70	36.81	95.10	10.30	43.09	9.18	0.76	19.23	5.85	67.47	25.20	114.96	24.30	224.04	44.33
DHLTNK12-71	0.57	10.65	0.25	2.35	4.33	0.63	28.03	9.94	116.98	46.48	209.07	42.82	387.86	76.16
DHLTNK12-72	0.06	1.53	0.14	2.57	9.98	0.25	74.33	31.03	406.93	154.93	661.57	127.52	1069.03	184.61
DHLTNK12-73	55.19	128.59	16.50	81.07	23.55	0.46	50.11	13.39	142.62	48.89	205.60	40.86	359.21	66.70
DHLTNK12-74	0.13	38.10	0.24	3.51	5.12	1.61	23.75	7.37	85.45	30.66	133.10	27.80	252.17	48.16
DHLTNK12-75	0.47	3.72	0.39	5.75	10.30	0.07	37.51	8.56	77.49	22.14	77.46	13.93	110.52	19.14
DHLTNK12-79	3.11	46.29	0.80	5.02	4.70	0.95	20.15	6.06	63.16	20.58	87.15	17.61	165.66	32.38
DHLTNK12-80	0.17	3.14	0.21	3.97	8.36	0.25	51.18	18.14	203.51	69.53	266.58	49.46	407.81	73.57
DHLTNK12-81	0.12	6.14	0.11	1.68	4.06	0.41	17.97	6.14	71.00	26.30	112.50	22.64	200.89	38.95
DHLTNK12-82	0.04	6.37	0.24	4.90	11.81	3.58	88.67	31.02	374.63	139.46	583.19	112.80	948.92	176.89
DHLTNK12-84	0.62	23.60	0.55	5.18	7.42	3.34	38.51	12.65	146.52	54.68	250.44	55.95	548.82	112.27
DHLTNK12-85	1.96	18.29	0.67	5.14	5.12	1.51	20.77	6.56	73.65	27.38	120.83	25.15	238.81	48.26
DHLTNK12-87	0.02	17.72	0.11	1.77	2.83	0.75	13.31	4.15	50.31	18.70	87.88	19.71	192.69	40.36
DHLTNK12-88	0.03	12.23	0.06	1.95	3.41	0.53	18.26	6.15	74.26	27.94	124.56	26.48	240.89	46.28
DHLTNK12-89	0.07	5.08	0.28	4.70	11.00	5.24	60.91	19.87	215.48	76.09	329.18	67.69	623.30	124.37
DHLTNK12-91	0.12	7.74	0.21	3.11	5.57	1.28	24.27	8.21	95.78	35.14	155.77	33.37	312.34	61.85
DHLTNK12-93	0.10	3.78	0.10	1.92	3.08	0.64	17.37	5.45	59.36	22.00	97.21	20.55	193.93	38.40
DHLTNK12-96	0.06	21.68	0.04	0.49	1.43	0.57	8.59	2.89	33.03	12.84	63.44	15.31	160.48	34.72
DHLTNK12-97	48.30	129.77	17.63	86.84	26.24	3.09	65.84	17.89	187.68	64.55	264.30	51.90	452.29	84.40
DHLTNK12-98	0.71	19.52	0.39	4.43	5.83	1.66	33.16	11.19	135.65	49.54	217.71	46.53	427.13	79.12

References

Adekoya, J.A., 1998. The geology and geochemistry of the Maru banded iron-formation, northwestern Nigeria. J. Afr. Earth Sc. 27, 241–257.

Alexandrov, E.A., 1973. The Precambrian banded iron-formations of the Soviet Union. Econ. Geol. 68, 1035–1062.

Babinski, M., Boggiani, P.C., Trindade, R.I.F., Fanning, C.M., 2013. Detrital zircon ages and geochronological constraints on the Neoproterozoic Puga diamictites and associated BIFs in the southern Paraguay Belt, Brazil. Gondwana Res. 23 (3), 988–997.

Basta, F.F., Maurice, A.E., Fontbote, L., Favarger, P.Y., 2011. Petrology and geochemistry of the banded iron formation (BIF) of Wadi Karim and Um Anab, Eastern Desert, Egypt: implications for the origin of Neoproterozoic BIF. Precambr. Res. 187 (3–4), 277–292.

Bekker, A., Krapez, B., Slack, J.F., Planavsky, N., Hofmann, A., Konhauser, K.O., Rouxel, O.J., 2012. Iron formation: the sedimentary product of the complex interplay among mantle, tectonic, oceanic, and biospheric processes – a reply. Econ. Geol. 107, 379–380.

Bekker, A., Planavsky, N.J., Krapez, B., Hofmann, A., Slack, J.F., Rouxel, O.J., Konhauser, K.O., 2014. Iron formations: their origins and implications for ancient seawater chemistry. Treatise Geochem. 9, 561–628 (second ed.).

Bekker, A., Slack, J.F., Planavsky, N., Krapež, B., Hofmann, A., Konhauser, K.O., Rouxel, O.J., 2010. Iron formation: the sedimentary product of a complex interplay among mantle, tectonic, oceanic, and biospheric processes. Econ. Geol. 105, 467–508.

Belousova, E.A., Griffin, W.L., O'Reilly, S.Y., Fisher, N.I., 2002. Igneous zircon: trace element composition as an indicator of source rock type. Contrib. Mineral. Petrol. 143, 602–622.

Belousova, E.A., Griffin, W.L., Pearson, N.J., 1998. Trace element composition and cathodoluminescence properties of southern African kimberlitic zircons. Mineral. Mag. 62, 355–366.

Bian, X.W., Zhu, H.P., Ji, W.H., Cui, J.T., Luo, Q.Z., Ren, J.G., Peng, X.P., 2013. The discovery of Qingbaikouan plutonite in Taxorgan, Xinjiang, and evidence from zircon LA-ICP-MS U–Pb dating of intrusive rock. Northwestern Geol. 46 (1), 22–31 (in Chinese with English abstract).

Canfield, D.E., Poulton, S.W., Knoll, A.W., Narbonne, G.M., Ross, G., Goldberg, T., Strauss, H., 2008. Ferruginous conditions dominated later Neoproterozoic deepwater chemistry. Science 321 (5891), 949–952.

Canfield, D.E., Poulton, S.W., Narbonne, G.M., 2007. Late Neoproterozoic deep-ocean oxygenation and the rise of animal life. Science 315, 92–95.

Chen, D.H., Wu, Y.Z., Li, W.M., Wang, X.A., Qiao, G.B., Zhao, X.J., 2013. Geological characteristics and genesis of the iron deposits in the Taxkorgan area. West Kunlun. Geotectonica et Metallogenia 37 (4), 671–684 (in Chinese with English abstract).

Condie, K.C., Belousova, E., Griffin, W.L., Sircombe, K.N., 2009. Granitoid events in space and time: constraints from igneous and detrital zircon age spectra. Gondwana Res. 15, 228–242.

Corfu, F., Hanchar, J.M., Hoskin, P.W.O., Kinny, P., 2003. Altas of zircon textures. Rev. Mineral. Geochem. 53, 469–500.

Cox, G.M., Halverson, G.P., Minarik, W.G., Heron, D.P.L., Macdonald, F.A., Bellefroid, E.J., Strauss, J.V., 2013. Neoproterozoic iron formation: an evaluation of its temporal, environment al and tectonic significance. Chem. Geol. 362, 232–249.

Cui, J.T., Wang, J.C., Bian, X.W., Peng, H.L., Yang, K.J., Zhu, H.P., 2005. The Qingbaikou stromatolites from the Tianshuihai Group complex in the Karakorum region, Xinjiang. Sedimentary Geol. Tethyan Geol. 25 (1–2), 194–197 (in Chinese with English abstract).

Dong, X., Zhang, Z.M., Santosh, M., Wang, W., Yu, F., Liu, F., 2011. Late Neoproterozoic thermal events in the northern Lhasa terrane, south Tibet: zircon chronology and tectonic implications. J. Geodyn. 52, 389–405.

Dong, Y.G., Guo, K.Y., Xiao, H.L., Zhang, C.L., Zhao, Y., 2004. Ore-forming conditions and prospecting in the West Kunlun area, Xinjiang, China. Acta Geol. Sin. 78 (2), 345–351 (English ed.).

Freitas, B.T., Warren, L.V., Boggiani, P.C., DeAlmeida, R.P., Piacentini, T., 2011. Tectono-sedimentary evolution of the Neoproterozoic BIF-bearing Jacadigo Group, SW-Brazil. Sedimentary Geol. 238 (1–2), 48–70.
Gaetani, M., Gosso, G., Pognante, U., 1990. A geological transect from Kunlunto Karakorum (Sinkiang, China): the western termination of the Tibetan Plateau. Preliminary note. Terra Nova 2, 23–30.
Ge, R.F., Zhu, W.B., Zheng, B.H., Wu, H.L., He, J.W., Zhu, X.Q., 2012. Early Pan-African magmatism in the Tarim Craton: insights from zircon U–Pb–Lu–Hf isotope and geochemistry of granitoids in the Korla area, NW China. Precambrian Res. 212–213, 117–138.
Geisler, T., Ulonska, M., Schleicher, H., Pidgeon, R.T., Bronswijk, W., 2001. Leaching and differential recrystallization of metamict zircon under experimental hydrothermal conditions. Chem. Geol. 141, 53–65.
Goodwin, A.M., 1962. Structure, stratigraphy and origin of iron formations, Michipicoten area, Algoma District, Ontario, Canada. Geol. Soc. Am. Bull. 73, 561–586.
Gross, G.A., 1991. Genetic concepts for iron-formation and associated metalliferous sediments. Ecol. Monogr. 8, 51–81.
Gross, G.A., Mcleod, C.R., 1980. A preliminary assessment of the chemical composition of iron formation in Canada. Can. Mineral. 18, 223–229.
Gutzmer, J., Mukhopadhyay, J., Beukes, N.J., Pack, A., Hayashi, K., Sharp, Z.D., 2006. Oxygen isotope composition of hematite and genesis of high-grade BIF-hosted iron ores. Geol. Soc. Am. Mem. 198, 257–268.
Halverson, G.P., Poitrasson, F., Hoffman, P.F., Nédélec, A., Montel, J.M., Kirby, J., 2011. Fe isotope and trace element geochemistry of the Neoproterozoic syn-glacial Rapitan iron formation. Earth Planet. Sci. Lett. 309 (1), 100–112.
Hayashi, K.I., Naraoka, H., Ohmoto, H., 2007. Oxygen isotope study of Paleoproterozoic banded iron formation, Hamersley Basin, Western Australia. Resour. Geol. 58, 43–51.
He, S.P., Li, R.S., Wang, C., Zhang, H.F., Ji, W.H., Yu, P.S., Gu, P.Y., Shi, C., 2011. Discovery of ~4.0 Ga detrital zircons in the Changdu Block, North Qiangtang, Tibetan Plateau. Sci. China Earth Sci. 56 (7), 647–658.
He, W.J., Zhu, W.B., Ge, R.F., Zheng, B.H., Wu, H.L., 2014. Detrital zircon U–Pb ages and Hf isotopes of Neoproterozoic strata in the Aksu area, northwestern Tarim Craton: implications for supercontinent reconstruction and crustal evolution. Precambr. Res. 254, 194–209.
Hoffman, P.F., Schrag, D.P., 2002. The snowball earth hypothesis: testing the limits of global change. Terra Nova 14 (3), 129–155.
Hofmann, A., Dirks, P.H.G.M., Jelsma, H.A., Matura, N., 2003. A tectonic origin for ironstone horizons in the Zimbabwe craton and their significance for greenstone belt geology. J. Geol. Soc. Lond. 160, 83–97.
Holland, H.D., 1973. The oceans, a possible source of iron-formations. Econ. Geol. 68, 1169–1172.
Hoskin, P.W.O., Black, L.P., 2000. Metamorphic zircon formation by solid-state recrystallization of protolith igneous zircon. J. Metamorph. Geol. 18, 423–439.
Hoskin, P.W.O., Ireland, T.R., 2000. Rare earth element chemistry of zircon and its use as a provenance indicator. Geology 7, 627–630.
Hoskin, P.W.O., Kinny, P.D., Wyborn, D., Chappell, B.W., 2000. Identifying accessory mineral saturation during differentiation in granitoid magmas: an integrated approach. J. Petrol. 41, 365–1396.
Hoskin, P.W.O., Schaltegger, U., 2003. The composition of zircon and igneous and metamorphic petrogenesis. Rev. Mineral. Geochem. 53, 27–55.
Huang, C.Y., 2014. Geological characteristics and genesis of the iron ore deposit in the Bulunkuole Group, West Kunlun, Xinjiang: Unpubl. PhD thesis, Guangzhou institute of Geochemistry Chinese Academy of Sciences, China (in Chinese with English abstract).
Huston, D.L., Logan, G.A., 2004. Barite, BIFs and bugs: evidence for the evolution of the Earth's early hydrosphere. Earth Planet. Sci. Lett. 220, 41–55.
Ilyin, A.V., 2009. Neoproterozoic banded iron formations. Lithol. Min. Resour. 44, 78–86.
Isley, A.E., Abbott, D.H., 1999. Plume-related mafic volcanism and the deposition of banded iron formation. J. Geophys. Res.: Atmos. 104, 461–477.
James, H.L., Sims, P.K., 1973. Precambrian iron-formations of the world: introduction. Econ. Geol. 68, 913–914.
James, H.R., 1954. Sedimentary facies of iron-formation. Econ. Geol. 49 (3), 235–293.
Ji, W.H., Li, R.S., Chen, S.J., He, S.P., Zhao, Z.M., Bian, X.W., Zhu, H.P., Cui, J.G., Ren, J.G., 2011. The discovery of Paleoproterozoic volcanic rocks in the Bulunkuoler Group from the Tianshuihai Massif in Xinjiang of Northwest China and its geological significance. Sci. China Earth Sci. 54, 61–72 (in Chinese).
Jiang, Y.H., Jia, R.Y., Liu, Z., Liao, S.Y., Zhao, P., Zhou, P., 2013. Origin of middle Triassic high-K calc-alkaline granitoids and their potassic microgranular enclaves from the Western Kunlun orogen, northwest China: a record of the closure of Paleo-Tethys. Lithos 156–159, 13–30.
Jiang, Y.H., Jiang, S.Y., Ling, H.F., Zhou, X.R., Rui, X.J., Yang, W.Z., 2002. Petrology and geochemistry of shoshonitic plutons from the Western Kunlun orogenic belt, northwestern Xinjiang, China: implications for granitoid geneses. Lithos 63, 165–187.
Johnston, D.T., Poulton, S.W., Dehler, C., Porter, S., Husson, J., Canfield, D.E., Knoll, A. H., 2010. An emerging picture of Neoproterozoic ocean chemistry: insights from the Chuar Group, Grand Canyon, USA. Earth Planet. Sci. Lett. 290, 64–73.
Johnston, D.T., Poulton, S.W., Goldberg, T., Sergeev, V.N., Podkovyrov, V., Vorob'eva, N.G., Bekker, A., Knoll, A.H., 2012. Late Ediacaran redox stability and metazoan evolution. Earth Planet. Sci. Lett. 335–336, 25–35.
Kao, H., Gao, R., Rau, R.J., Shi, D., Chen, R.Y., Guan, Y., Wu, F.T., 2001. Seismic image of the Tarim basin and its collision with Tibet. Geology 29, 575–578.
Khalil, K.I., El-Shazly, A.K., 2012. Petrological and geochemical characteristics of Egyptian banded iron formations: review and new data from Wadi Kareim. Geochemistry 12, 105–126.
Kimberley, M.M., 1989. Exhalative origins of iron formations. Ore Geol. Rev. 5, 13–145.
Klein, C., 2005. Some Precambrian banded iron-formations (BIFs) from around the world: their age, geologic setting, mineralogy, metamorphism, geochemistry, and origins. Am. Mineral. 90 (10), 1473–1499.
Klein, C., Beukes, N.J., 1989. Geochemistry and sedimentology of a facies transition from limestone to iron-formation deposition in the Early Proterozoic Transvaal Supergroup, South Africa. Econ. Geol. 84 (7), 1733–1774.
Klein, C., Beukes, N.J., 1992. Time distribution, stratigraphy, sedimentologic setting, and geochemistry of Precambrian iron-formations. In: Schopf, J.W., Klein, C. (Eds.), The Proterozoic Biosphere. Cambridge University Press, Cambridge, pp. 139–146.
Klein, C., Beukes, N.J., 1993. Sedimentology and geochemistry of the glaciogenic Late Proterozoic rapitan iron-formation in Canada. Econ. Geol. 88, 542–565.
Klein, C., Ladeira, E.A., 2000. Geochemistry and petrology of some Proterozoic banded iron-formations of the Quadrílatero Ferrífero, Minas Gerais, Brazil. Econ. Geol. 95, 405–428.
Klein, C., Ladeira, E.A., 2004. Geochemistry and mineralogy of Neoproterozoic banded iron-formations and some selected, siliceous manganese formations from the Urucum district, Mato Grosso do Sul, Brazil. Econ. Geol. 99, 1233–1244.
Kuang, W.L., Liu, J.S., Zhu, Z.Q., Li, S.H., 2002. Metallogenesis of Kalangu MVT type lead-zinc deposit and sources of minerogenetic materials in West Kunlun. Geotectonica et Metallogenia 26 (4), 423–428 (in Chinese with English abstract).
Kump, L.R., Seyfried Jr., W.E., 2005. Hydrothermal Fe fluxes during the Precambrian: effect of low oceanic sulphate concentrations and low hydrostatic pressure on the composition of black smokers. Earth Planet. Sci. Lett. 235 (3–4), 654–662.
Li, H.M., Zhang, Z.J., Li, L.X., Zhang, Z.C., Chen, J., Yao, T., 2014. Types and general characteristics of the BIF-related iron deposits in China. Ore Geol. Rev. 57, 264–287.
Li, R.S., Ji, W.H., Yang, Y.C., 2008. Geology of Kunlun Mountains and Adjacent Areas. Geological Publishing House, Beijing (in Chinese).
Liou, J.G., Kuniyoshi, S., Ito, K., 1974. Experimental studies of the phase relations between greenschist and amphibolite in a basaltic system. Am. J. Sci. 274, 613–632.
Liu, J.P., Wang, H., Li, S.H., Tong, L.X., Ren, G.L., 2010. Geological and geochemical features and geochronology of the Kayizi porphyry molybdenum deposit in the northern belt of West Kunlun, NW China. Acta Geol. Sin. 26 (10), 3095–3105 (in Chinese with English abstract).
Liu, Y.S., Hu, Z.C., Gao, S., Gunther, D., Xu, J., Gao, C.G., Chen, H.H., 2008. In situ analysis of major and trace elements of anhydrous minerals by LA-ICP-MS without applying an internal standard. Chem. Geol. 257, 34–43.
Liu, Z., Jiang, Y.H., Jia, R.Y., Zhao, P., Zhou, Q., 2015. Origin of Late Triassic high-K calc-alkaline granitoids and their potassic microgranular enclaves from the western Tibet Plateau, northwest China: implications for Paleo-Tethys evolution. Gondwana Res. 27, 326–341.
Lottermoser, B.G., Ashley, P.M., 2000. Geochemistry, petrology and origin of Neoproterozoic iron-stones in the eastern part of the Adelaide Geosycline, South Australia. Precambr. Res. 101, 49–67.
Ludwig, K.R., 2003. User's Manual for Isoplot 3.00. A Geochronological Toolkit for Microsoft Excel, Berkeley Geochronology Centre. Special Publication, Berkeley, CA, No. 4a.
Luo, J.H., Che, Z.C., Zhang, X.L., Han, W., Zhang, G.F., Nian, X., 2011. Neoproterozoic granitoid magmatism in the Kuqe depression of northeastern Tarim Basin and its significance. Acta Geol. Sinica 85, 467–474 (in Chinese with English abstract).
Ma, X.X., Shu, L.S., Jahn, B.M., Zhu, W.B., Faure, M., 2012a. Precambrian tectonic evolution of Central Tianshan, NW China: constraints from U–Pb dating and in situ Hf isotopic analysis of detrital zircons. Precambr. Res. 222–223, 450–473.
Ma, X.X., Shu, L.S., Santosh, M., Li, J.Y., 2012b. Detrital zircon U–Pb geochronology and Hf isotope data from Central Tianshan suggesting a link with the Tarim Block: implications on Proterozoic supercontinent history. Precambr. Res. 206–207, 1–16.
Maas, R., Kinny, P.D., Williams, I.S., Froude, D.O., Compston, W., 1992. The Earth's oldest known crust: a geochronological and geochemical study of 3900–4200 Ma old detrital zircons from Mt. Narryer and Jack Hills, Western Australia. Geochimica et Cosmochimica Acta 56, 1281–1300.
Matte, P., Tapponnier, P., Bourjot, L., Pan, Y., Wang, Y., 1992. Tectonics of western Tibet, from the Kunlun to the Karakorum. International Symposium on the Karakorum and Kunlun Mountains, Abstracts, June 1992, Kashi, 36.
Matte, Ph., Tapponnier, P., Arnaud, N., Bourjot, L., Avouac, J.P., Vidal, Ph., Liu, Q., Pan, Y.S., Wang, Y., 1996. Tectonics of Western Tibet, between the Tarim and the Indus. Earth Planet. Sci. Lett. 142, 311–330.
Mattern, F., Schneider, W., 2000. Suturing of the Proto- and Paleo-Tethys oceans in the Western Kunlun (Xijiang, China). J. Asian Earth Sci. 18, 637–650.
Mattern, F., Schneider, W., Li, Y., Li, X., 1996. A traverse through the Western Kunlun (Xinjiang, China): tentative geodynamic implications for the Paleozoic and Mesozoic. Geol. Rundsch. 85, 705–722.
Pan, G.T., Zhu, D.C., Wang, L.Q., Liao, Z.L., Geng, Q.R., Jiang, X.S., 2004. Banggong Lake-Nu River suture zone-the northern boundary of Gondwanaland: evidence from geology and geophysics. Earth Sci. Front. 11 (4), 371–382 (in Chinese with English abstract).

Pan, Y., Wang, Y., Matte, Ph., Tapponnier, P., 1994. Tectonic evolution along the geotraverse from Yecheng to Shiquanhe. Acta Geol. Sin. 68, 295–307 (in Chinese with English abstract).
Pan, Y.S., 1996. Geological Evolution of the Karakorum and Kunlun Mountains. Seismological Press, Beijing (in Chinese).
Pickard, A.L., 2003. SHRIMP U–Pb zircon ages for the Paleoproterozoic Kuruman iron formation, Northern Cape Province, South Africa: evidence for simultaneous BIF deposition on Kaapvaal and Pilbara cratons. Precambr. Res. 125, 275–315.
Pirajno, F., 2013. The Geology and Tectonic Settings of China's Mineral Deposits. Springer, Part of Springer Science + Business Media.
Rasmussen, B., Fletcher, I.R., Bekker, A., Muhling, J.R., Gregory, C.J., Thorne, A.M., 2012. Deposition of 1.88-billion-year-old iron formations as a consequence of rapid crustal growth. Nature 484, 498–501.
Ravikant, V., Wu, F.Y., Ji, W.Q., 2011. U–Pb age and Hf isotopic constraints of detrital zircons from the Himalayan foreland Subathu sub-basin on the Tertiary paleogeography of the Himalaya. Earth Planet. Sci. Lett. 304, 356–368.
Rino, S., Kon, Y., Sato, W., Maruyama, S., Santosh, M., Zhao, D., 2008. The Grenvillian and Pan-African orogens: world's largest orogenies through geologic time, and their implications on the origin of superplume. Gondwana Res. 14, 51–72.
Rubatto, D., 2002. Zircon trace element geochemistry: partitioning with garnet and the link between U–Pb ages and metamorphism. Chem. Geol. 184, 123–138.
Schreiber, H.D., Lauer, H.V., Thanyasir, T., 1980. The redox state of cerium in basaltic magmas: an experimental study of iron-cerium interactions in silicate melts. Geochim. Cosmochim. Acta 44, 1599–1612.
Shields, Z.G., Och, L., 2011. The case for a Neoproterozoic oxygenation event: geochemical evidence and biological consequences. GSA Today 12 (3), 4–11.
Shu, L.S., Deng, X.L., Zhu, W.B., Ma, D.S., Xiao, W.J., 2011. Precambrian tectonic evolution of the Tarim block, NW China: new geochronological insights from the Quruqtagh domain. J. Afr. Earth Sc. 42 (5), 774–790.
Spier, C.A., de Oliveira, S.M.B., Rosière, C.A., 2003. Geology and geochemistry of the Águas Claras Quadrilátero Ferrífero, Minas Gerais, Brazil. Miner. Deposita 38, 751–774.
Spier, C.A., de Oliveira, S.M.B., Sial, A.N., Rios, F.J., 2007. Geochemistry and genesis of the banded iron formations of the Cauê Formation, Quadrilátero Ferrífero, Minas Gerais, Brazil. Precambr. Res. 152, 170–206.
Stern, R.J., Mukherjee, S.K., Nathan, R.M., Kamal, A., Peter, R.J., 2013. 750 Ma banded iron formation from the Arabian-Nubian Shield – implications for understanding Neoproterozoic tectonics, volcanism, and climate change. Precambr. Res. 239, 79–94.
Sun, H.T., Wu, J.R., Yu, P.S., Li, J.P., 1998. Geology, geochemistry and sulfur isotope composition of the Late Proterozoic Jingtieshan (Superior-type) hematite–jasper–barite iron ore deposits associated with strata-bound Cu mineralization in the Gansu Province, China. Miner. Deposita 34, 102–112.
Sun, S.S., McDonough, W.F., 1989. Chemical and isotopic systematics of oceanic basalts: implications for mantle composition and processes. Geol. Soc. Lond. Spec. Publ. 42, 313–345.
Tang, J.F., Fu, H.Q., Yu, Z.Q., 1987. Stratigraphy, type and formation conditions of the Precambrian banded iron ores in south China. Chin. J. Geochem. 6 (4), 331–341.
Taylor, D., Dalstra, H.J., Harding, A.E., Broadbent, G.C., Barley, M.E., 2001. Genesis of high-grade hematite orebodies of the Hamersley province, Western Australia. Econ. Geol. 96, 837–873.
Thorne, W., Hagemann, S., Vennemann, T., Oliver, N., 2009. Oxygen isotope compositions of iron oxides from high-grade BIF-hosted iron ore deposits of the Central Hamersley Province, Western Australia: constraints on the evolution of hydrothermal fluids. Econ. Geol. 104, 1019–1035.
Trendall, A.F., Blockley, J.G., 1970. The Iron-formations of the Precambrian Hamersley Group, Western Australia, vol. 119. Geological Survey of Western Australia, p. 366.
Volkert, R.A., Monteverde, D.H., Friehauf, K.C., Gates, A.E., Dalton, R.F., Smith II, R.C., 2010. Geochemistry and origin of Neoproterozoic ironstone deposits in the New Jersey Highlands and implications for the eastern Laurentian rifted margin in the north-central Appalachians, USA. Geol. Soc. Am. Mem. 206, 283–306.
Wang, C., 2011. Precambrian tectonic of south margin of Tarim basin, NW China: Ph. D thesis, Northwest University, China (in Chinese with English abstract).
Wang, J.P., 2008. Geological features and tectonic significance of mélange zone in West Kunlun Taxkorgan: publ. Ph. D thesis, China University of Geoscience (in Chinese with English abstract).
Wang, Y.Z., 1983. The age of the Yisak Group of West Kunlun, and tectonic significance. Xinjiang Geol. 1 (1), 1–8 (in Chinese with English abstract).
Whitehouse, M.J., Platt, J.P., 2003. Dating high-grade metamorphism constraints from rare-earth elements in zircons and garnet. Contrib. Miner. Petrol. 145, 61–74.
Xiao, W.J., Han, F.L., Windley, B.F., Yuan, C., Zhou, L., Li, J.L., 2003. Multiple accretionary orogenesis and episodic growth of continents: insights from the Western Kunlun Range, central Asia. Int. Geol. Rev. 45, 303–328.
Xiao, W.J., Pirajno, F., Windley, B.F., Han, C.M., 2006. Paleozoic-early Mesozoic accretionary tectonics and metallogeny of the northern Tibetan Plateau Extended Abs, IAGOD Meeting, Moscow.
Xiao, W.J., Windley, B.F., Hao, J., Li, J.L., 2002. Arc-ophiolite obduction in the Western Kunlun Range (China): implications for the Paleozoic evolution of central Asia. J. Geol. Soc. 159, 517–528.
Xiao, W.J., Windley, B.F., Liu, D.Y., Jian, P., Liu, C.Z., Yuan, C., Sun, M., 2005. Accretionary tectonics of the Western Kunlun orogen, China: a Paleozoic–Early Mesozoic, long lived active continental margin with implications for the growth of southern Eurasia. J. Geol. 113, 687–705.
Xu, D.R., Wang, Z.L., Cai, J.X., Wu, C.J., Bakun-Czubarow, N., Wang, L., Chen, H.Y., Baker, M.J., Kusiak, M.A., 2013. Geological characteristics and metallogenesis of the Shilu Fe-ore deposit in Hainan Provinces, South China. Ore Geol. Rev. 53, 318–342.
Xu, D.R., Wang, Z.L., Chen, H.Y., Hollings, P., Jansen, N.H., Zhang, Z.C., Wu, C.J., 2014. Petrography and geochemistry of the Shilu Fe–Co–Cu ore district, South China: implications for the origin of a Neoproterozoic BIF system. Ore Geol. Rev. 57, 322–350.
Xu, D.R., Xiao, Y., Xia, B., Cai, R.J., Hou, W., Wang, L., Liu, Z.L., Zhao, B., 2009. Metallogenic Model and Ore Predicating of the Shilu Iron Ore Deposit in Hainan Province. Geology Publishing House, Beijing, China (in Chinese).
Yan, C.H., Chen, C.J., Cao, X.Z., Zhang, W.S., Chen, J.K., Li, S.B., Liu, P.D., 2012. The discovery of the Pamir-type iron deposits in Taxkorgan area of Xinjiang and its geological significance. Geol. Bull. China 31 (4), 549–557 (in Chinese with English abstract).
Yang, D.B., Xu, W.L., Xu, Y.G., Wang, Q.H., Pei, F.P., Wang, F., 2012. U–Pb ages and Hf isotope data from detrital zircons in the Neoproterozoic sandstones of northern Jiangsu and southern Liaoning Provinces, China: implications for the Late Precambrian evolution of the southeastern North China Craton. Precambr. Res. 216–219, 162–176.
Yao, J.L., Shu, L.S., Santosh, M., 2011. Detrital zircon U–Pb geochronology, Hf-isotopes and geochemistry – new clues for the Precambrian crustal evolution of Cathaysia Block, South China. Gondwana Res. 20, 553–567.
Young, G.M., 2002. Stratigraphic and tectonic settings of Proterozoic glaciogenic rocks and banded iron-formations: relevance to the snowball Earth debate. J. Afr. Earth Sc. 35, 451–466.
Yuan, C., Sun, M., Zhou, M.F., Zhou, H., Xiao, W.J., Li, J.L., 2003. Absence of Archean basement in the South Kunlun Block: Nd–Sr–O isotopic evidence from granitoids. Island Arc 12, 13–21.
Yuan, C., Sun, M., Zhou, M.F., Zhou, H., Xiao, W.J., Li, J.L., 2002. Tectonic evolution of the West Kunlun: geochronologic and geochemical constraints from Kudi granitoids. Int. Geol. Rev. 44, 653–669.
Zhai, M.G., Windley, B.F., 1990. The Archean and Early Proterozoic banded iron formations of North China: their characteristics, geotectonic relations, chemistry and implications for crustal growth. Precambr. Res. 48, 267–286.
Zhang, C.L., Dong, Y.G., Zhao, Y., 2003c. Geochemistry of Mesoproterozoic volcanics in West Kunlun: evidence for the plate tectonic evolution. Acta Geol. Sinica 78, 532–542 (English ed.).
Zhang, C.L., Li, Z.X., Li, X.H., Ye, H.M., 2009. Neoproterozoic mafic dyke swarms at the northern margin of the Tarim block, NW China: age, geochemistry, petrogenesis and tectonic implications. J. Asian Earth Sci. 35, 167–179.
Zhang, C.L., Lu, S.N., Yu, H.F., Ye, H.M., 2007. Tectonic evolution of the Western Kunlun orogenic belt in the northern margin of the Tibetan Plateau: evidence from SHRIMP and LA-ICP-MS Zircon dating. Sci. China Earth Sci. 37 (2), 145–154 (in Chinese).
Zhang, C.L., Wang, Z.G., Shen, J.L., Bi, H., Guo, K.Y., Wang, A.G., 2003b. Zircon SHRIMP dating and geochemistry characteristics of Akazi rock mass of Western Kunlun. Acta Geol. Sinica 19 (3), 523–529 (in Chinese with English abstract).
Zhang, C.L., Y, C., Shen, J.L., Wang, A.G., Zhao, Y., Dong, Y.G., Guo, K.Y., 2003d. Zircon SHRIMP age of Neoproterozoic gneiss granites in the West Kunlun and its significance. Geol. Rev. 19 (3), 239–244 (in Chinese with English abstract).
Zhang, C.L., Zhao, Y., Guo, K.Y., Dong, Y.G., Wang, A.G., 2003a. Grenville orogeny in north of the Qinghai-Tibet plateau: first evidence from isotopic dating. Chin. J. Geol. 38 (4), 535–538 (in Chinese with English abstract).
Zhang, L.C., Zhai, M.G., Zhang, X.J., Xiang, P., Dai, Y.P., Wang, C.L., Pirajno, F., 2012a. Formation age and tectonic setting of the Shirengou Neoarchean banded iron deposit in eastern Hebei province: constraints from geochemistry and SIMS zircon U–Pb dating. Precambr. Res. 222–223, 325–338.
Zhang, X.J., Zhang, L.C., Xiang, P., Wan, B., Pirajno, F., 2011. Zircon U–Pb age, Hf isotopes and geochemistry of Shuichang Algoma-type banded iron formation, North China Craton: constraints on the ore-forming age and tectonic setting. Gondwana Res. 20, 137–148.
Zhang, Y.Q., Xie, Y.W., 1989. A study on the Rb–Sr biotite isochron ages of the granitoid in the Sanshiliyingfang area of the Karakoram and Kunlun Mts. Region. J. Nat. Resour. 4 (3), 222–227 (in Chinese with English abstract).
Zhang, Z.M., Dong, X., Liu, F., Lin, Y.H., Yan, R., He, Z.Y., Santosh, M., 2012b. The making of Gondwana: discovery of 650 Ma HP granulites from the North Lhasa, Tibet. Precambrian Res. 212–213, 107–116.
Zhou, H., 1998. The main ductile shear zone and the lithosphere effective elastic thickness of West Kunlun orogenic belt: Unpubl. PhD thesis, Institute of Geology, Chinese Academy of Sciences, Beijing, China (in Chinese with English abstract).
Zhu, D.C., Zhao, Z.D., Niu, Y.L., Dilek, Y., Mo, X.X., 2011a. Lhasa terrane in southern Tibet came from Australia. Geology 39 (8), 727–730.
Zhu, W.B., Zhang, Z.Y., Shu, L.S., Lu, H.F., Su, J.B., Yang, W., 2008. SHRIMP U–Pb zircon geochronology of Neoproterozoic Korla mafic dykes in the northern Tarim Block, NW China: implications for the long-lasting breakup process of Rodinia. J. Geol. Soc. 165, 887–890.
Zhu, W.B., Zheng, B.H., Shu, L.S., Ma, D.S., Wan, J.L., Zheng, D.W., Zhang, Z.Y., Zhu, X. Q., 2011b. Geochemistry and SHRIMP U–Pb zircon geochronology of the Korla mafic dykes: constrains on the Neoproterozoic continental breakup in the Tarim block, northwest China. J. Asian Earth Sci. 42, 791–804.